# Chapter 10

# Beam/Ray Imaging

JOACHIM NAGEL
Department of Biomedical Engineering
University of Miami
Coral Gables, Florida



## INTRODUCTION I

The diagnosis of disease is facilitated by imaging internal structures of anatomy and metabolic processes. The basic medical imaging techniques are

radiographic (X-ray) imaging,
nuclear medicine (gamma-ray) imaging,



HANDBOOK OF BIOMEDICAL ENGINEERING

magnetic resonance imaging (MRI),
ultrasound (US) imaging, and
endoscopy.

With the exception only of ultrasonic imaging, these techniques use electromagnetic waves as information carriers or measuring probes. According to the nature and wavelength of the radiation used and the properties of its interaction with tissue, including its ability to penetrate, specific diagnostic applications and imaging principles have been developed for each type of radiation [1–3,34,35].

Conventional radiography, the most used technique, is based on imaging two-dimensional (2-D) projections of tissue absorption or radiopacity, as obtained by recording the intensity modulation of X rays penetrating the body. Due to the variance of absorption coefficients and spatial dimensions, different types of tissue and organs become visible and discernable as the projection of anatomical structures onto the imaging plane. Important spatial information is lost in the projection, so reconstruction techniques, known as X-ray computed tomography, have been developed to generate true 2-D sectional views of single tissue layers from a multitude of projections. Successive sectional views can be combined to compute sectional views with various arbitrary orientations or even to generate 3-D images.

Nuclear medicine imaging also provides information on anatomical structure, but its essential feature is to visualize metabolic processes, thus introducing a new dimension to medical diagnostic imaging. Metabolic imaging is achieved through the selective administration of radioactive materials, so that the region under study becomes a source of gamma rays, which can be displayed using techniques similar to those of radiography. Either the radioactive material itself or the chemical substance in which it is bound has properties that cause its selective concentration in specific regions of the body. Radioactive labeling of characteristic metabolic compounds (radiopharmaceuticals), allows the selective monitoring of physiological processes in the body. Image content is the spatial distribution of the radiating sources rather than the radiographic display of attenuation coefficients.

Magnetic resonance imaging (MRI) uses the paramagnetic properties of certain elements, such as hydrogen and phosphorus, to generate images of their densities, relaxation times, and chemical bonds, thus providing information on the morphology, histology, and metabolism of the tissue of which they are constituent. Image formation is based on the excitation of paramagnetic spin resonance by rf waves in the presence of a strong magnetic field, which causes characteristic induction signals that originate in the different volume elements of the body. Spatial coding of the

magnetic field causes space-dependent frequency and/or phase encoding of the measuring signals, thus providing 3-D image generation. A comprehensive analysis of NMR is presented in the next chapter.

Ultrasound (US) imaging is based upon visualization of acoustic properties, mainly the reflectivity boundaries, of tissue. The partial reflection of ultrasonic waves (echoes) at the interface between tissues with different acoustic impedances, enables the imaging of anatomical structures. Spectral analysis of the echo waves provides information on motion or flow, based on the Doppler shift of moving target reflections. Transmission mode measurements display a number of acoustic parameters such as attenuation, scattering, and velocity of propagation that can be related to tissue characterization, which improves the accuracy of diagnosis of heart diseases and cancerous tissue.

Endoscopy is the only imaging technique based on invasion of the body with an optical probe, either flexible fiber optics or miniaturized TV systems, which makes possible the direct imaging of inner structures. Although not as technically fascinating as the other imaging techniques, and not often mentioned, endoscopy has the tremendous diagnostic potential of supporting imaging with the ability to take samples for biopsy. Endoscopy also has great therapeutic potential, such as the ability to stop even major internal bleeding and to remove foreign objects.

## RADIOGRAPHIC IMAGING II

Radiography, the classical medical imaging technique routinely applied to nearly all hospitalized patients, whether or not there is a direct need, uses high-energy electromagnetic waves or photons (X rays), as a tool to "look" through the patient to obtain information on anatomical structures. The propagation of X rays, characterized by wavelengths that are shorter than the atomic diameters of the penetrated matter, is dominated by corpuscular ray properties rather than by the wave character of light. The velocity of propagation is essentially constant for all kinds of biological tissue; thus the refractive index of all such structures is unity. As a consequence, the only mechanisms of interaction are absorption and scattering: No reflection or diffraction takes place. So, unlike ultrasonic waves, X rays travel in straight lines through the body, unaffected by tissue interfaces, and provide undistorted images of high resolution [33].

The term radiography is sometimes misleading because it applies to various X-ray techniques. Its original definition referred only to the

magnetic resonance imaging (MRI),
ultrasound (US) imaging, and
endoscopy.

With the exception only of ultrasonic imaging, these techniques use electromagnetic waves as information carriers or measuring probes. According to the nature and wavelength of the radiation used and the properties of its interaction with tissue, including its ability to penetrate, specific diagnostic applications and imaging principles have been developed for each type of radiation [1–3,34,35].

Conventional radiography, the most used technique, is based on imaging two-dimensional (2-D) projections of tissue absorption or radiopacity, as obtained by recording the intensity modulation of X rays penetrating the body. Due to the variance of absorption coefficients and spatial dimensions, different types of tissue and organs become visible and discernable as the projection of anatomical structures onto the imaging plane. Important spatial information is lost in the projection, so reconstruction techniques, known as X-ray computed tomography, have been developed to generate true 2-D sectional views of single tissue layers from a multitude of projections. Successive sectional views can be combined to compute sectional views with various arbitrary orientations or even to generate 3-D images.

Nuclear medicine imaging also provides information on anatomical structure, but its essential feature is to visualize metabolic processes, thus introducing a new dimension to medical diagnostic imaging. Metabolic imaging is achieved through the selective administration of radioactive materials, so that the region under study becomes a source of gamma rays, which can be displayed using techniques similar to those of radiography. Either the radioactive material itself or the chemical substance in which it is bound has properties that cause its selective concentration in specific regions of the body. Radioactive labeling of characteristic metabolic compounds (radiopharmaceuticals), allows the selective monitoring of physiological processes in the body. Image content is the spatial distribution of the radiating sources rather than the radiographic display of attenuation coefficients.

Magnetic resonance imaging (MRI) uses the paramagnetic properties of certain elements, such as hydrogen and phosphorus, to generate images of their densities, relaxation times, and chemical bonds, thus providing information on the morphology, histology, and metabolism of the tissue of which they are constituent. Image formation is based on the excitation of paramagnetic spin resonance by rf waves in the presence of a strong magnetic field, which causes characteristic induction signals that originate in the different volume elements of the body. Spatial coding of the

magnetic field causes space-dependent frequency and/or phase encoding of the measuring signals, thus providing 3-D image generation. A comprehensive analysis of NMR is presented in the next chapter.

Ultrasound (US) imaging is based upon visualization of acoustic properties, mainly the reflectivity boundaries, of tissue. The partial reflection of ultrasonic waves (echoes) at the interface between tissues with different acoustic impedances, enables the imaging of anatomical structures. Spectral analysis of the echo waves provides information on motion or flow, based on the Doppler shift of moving target reflections. Transmission mode measurements display a number of acoustic parameters such as attenuation, scattering, and velocity of propagation that can be related to tissue characterization, which improves the accuracy of diagnosis of heart diseases and cancerous tissue.

Endoscopy is the only imaging technique based on invasion of the body with an optical probe, either flexible fiber optics or miniaturized TV systems, which makes possible the direct imaging of inner structures. Although not as technically fascinating as the other imaging techniques, and not often mentioned, endoscopy has the tremendous diagnostic potential of supporting imaging with the ability to take samples for biopsy. Endoscopy also has great therapeutic potential, such as the ability to stop even major internal bleeding and to remove foreign objects.

## RADIOGRAPHIC IMAGING II

Radiography, the classical medical imaging technique routinely applied to nearly all hospitalized patients, whether or not there is a direct need, uses high-energy electromagnetic waves or photons (X rays), as a tool to "look" through the patient to obtain information on anatomical structures. The propagation of X rays, characterized by wavelengths that are shorter than the atomic diameters of the penetrated matter, is dominated by corpuscular ray properties rather than by the wave character of light. The velocity of propagation is essentially constant for all kinds of biological tissue; thus the refractive index of all such structures is unity. As a consequence, the only mechanisms of interaction are absorption and scattering: No reflection or diffraction takes place. So, unlike ultrasonic waves, X rays travel in straight lines through the body, unaffected by tissue interfaces, and provide undistorted images of high resolution [33].

The term radiography is sometimes misleading because it applies to various X-ray techniques. Its original definition referred only to the

magnetic resonance imaging (MRI),
ultrasound (US) imaging, and
endoscopy.

With the exception only of ultrasonic imaging, these techniques use electromagnetic waves as information carriers or measuring probes. According to the nature and wavelength of the radiation used and the properties of its interaction with tissue, including its ability to penetrate, specific diagnostic applications and imaging principles have been developed for each type of radiation [1–3,34,35].

Conventional radiography, the most used technique, is based on imaging two-dimensional (2-D) projections of tissue absorption or radiopacity, as obtained by recording the intensity modulation of X rays penetrating the body. Due to the variance of absorption coefficients and spatial dimensions, different types of tissue and organs become visible and discernable as the projection of anatomical structures onto the imaging plane. Important spatial information is lost in the projection, so reconstruction techniques, known as X-ray computed tomography, have been developed to generate true 2-D sectional views of single tissue layers from a multitude of projections. Successive sectional views can be combined to compute sectional views with various arbitrary orientations or even to generate 3-D images.

Nuclear medicine imaging also provides information on anatomical structure, but its essential feature is to visualize metabolic processes, thus introducing a new dimension to medical diagnostic imaging. Metabolic imaging is achieved through the selective administration of radioactive materials, so that the region under study becomes a source of gamma rays, which can be displayed using techniques similar to those of radiography. Either the radioactive material itself or the chemical substance in which it is bound has properties that cause its selective concentration in specific regions of the body. Radioactive labeling of characteristic metabolic compounds (radiopharmaceuticals), allows the selective monitoring of physiological processes in the body. Image content is the spatial distribution of the radiating sources rather than the radiographic display of attenuation coefficients.

Magnetic resonance imaging (MRI) uses the paramagnetic properties of certain elements, such as hydrogen and phosphorus, to generate images of their densities, relaxation times, and chemical bonds, thus providing information on the morphology, histology, and metabolism of the tissue of which they are constituent. Image formation is based on the excitation of paramagnetic spin resonance by rf waves in the presence of a strong magnetic field, which causes characteristic induction signals that originate in the different volume elements of the body. Spatial coding of the

magnetic field causes space-dependent frequency and/or phase encoding of the measuring signals, thus providing 3-D image generation. A comprehensive analysis of NMR is presented in the next chapter.

Ultrasound (US) imaging is based upon visualization of acoustic properties, mainly the reflectivity boundaries, of tissue. The partial reflection of ultrasonic waves (echoes) at the interface between tissues with different acoustic impedances, enables the imaging of anatomical structures. Spectral analysis of the echo waves provides information on motion or flow, based on the Doppler shift of moving target reflections. Transmission mode measurements display a number of acoustic parameters such as attenuation, scattering, and velocity of propagation that can be related to tissue characterization, which improves the accuracy of diagnosis of heart diseases and cancerous tissue.

Endoscopy is the only imaging technique based on invasion of the body with an optical probe, either flexible fiber optics or miniaturized TV systems, which makes possible the direct imaging of inner structures. Although not as technically fascinating as the other imaging techniques, and not often mentioned, endoscopy has the tremendous diagnostic potential of supporting imaging with the ability to take samples for biopsy. Endoscopy also has great therapeutic potential, such as the ability to stop even major internal bleeding and to remove foreign objects.

## RADIOGRAPHIC IMAGING II

Radiography, the classical medical imaging technique routinely applied to nearly all hospitalized patients, whether or not there is a direct need, uses high-energy electromagnetic waves or photons (X rays), as a tool to "look" through the patient to obtain information on anatomical structures. The propagation of X rays, characterized by wavelengths that are shorter than the atomic diameters of the penetrated matter, is dominated by corpuscular ray properties rather than by the wave character of light. The velocity of propagation is essentially constant for all kinds of biological tissue; thus the refractive index of all such structures is unity. As a consequence, the only mechanisms of interaction are absorption and scattering: No reflection or diffraction takes place. So, unlike ultrasonic waves, X rays travel in straight lines through the body, unaffected by tissue interfaces, and provide undistorted images of high resolution [33].

The term radiography is sometimes misleading because it applies to various X-ray techniques. Its original definition referred only to the

recording of X-ray projection images on photographic film. Using a fluoroscopic screen as the X-ray detector (instead of film), called fluoroscopy, provided the ability of continuous X-ray monitoring. The use of TV systems for electronically monitoring the fluoroscopic screen is called X-ray television. Because all of these systems, including film recording, use fluoroscopic screens as image converters, and all of them are based on the same physical principle of imaging (i.e., the projection of body absorption onto a single plane), the terminology is illogical and arbitrary. So, with the development of the imaging principle called computed tomography (CT), a renaming took place, in which all possible imaging techniques using X rays are called radiography. CT, first realized only in X-ray imaging, become X-ray CT after its extension to MRI, US, and nuclear medicine imaging.

# A Physics of Radiographic Imaging

## 1 X Rays

X rays are generated by bombarding a metallic target with accelerated, high-energy electrons. Their interactions with the nucleus or the inner electron shell of the target atoms result in conversion of their kinetic energy to high-frequency electromagnetic radiation [19]. Two mechanisms contribute to the generation of X-rays depending on the type of interaction. The collision of an electron and a heavy nucleus results in a sharp deceleration and deflection of the electron. The lost kinetic energy is not transferred to the nucleus but, in accordance with the electrodynamics of decelerated charges, is converted to electromagnetic radiation: the bremsstrahlung or braking radiation. An ensemble of electrons striking the target produces a continuous spectrum of photon energies, since the varying distances of the electron trajectories to the target nuclei cause different amounts of kinetic energy to be converted to radiation, and some of the kinetic energy of electrons is lost by non-radiating collisions (e.g., with free electrons) prior to an X-ray generating interaction. The highest photon energy results from a central collision, in which all the kinetic energy of the impinging electron is emitted as radiation:

$$hf_{\mathrm{h}} = E_{\mathrm{kin}} \tag{1}$$

where $f_{\mathrm{h}}$ is the highest possible X-ray frequency, $h$ Planck's constant of action, and $E_{\mathrm{kin}}$ the kinetic energy of the electron.

The collision of an accelerated electron with an electron of the innermost shell of a target atom knocks the bound electron out of orbit. The replacement of the inner vacancy by an outer-shell electron produces a

photon with an energy corresponding to the difference between the two electronic energy levels. Therefore this component of the generated radiation is restricted to discrete frequencies that are typical of the target material and thus are called characteristic radiation.

A typical X-ray spectrum shows the continuous bremsstrahlung overlayed by the material-dependent peaks of the characteristic radiation, as can be seen in Fig. 1 for electrons of 100 keV impinging on a tungsten target. The energy distribution of the emitted X rays shows characteristic peaks at 57.9, 59.3, 67.4, and 69.3 keV, corresponding to wavelengths in the range of 20 pm.

Bremsstrahlung shows a wide range of energies, with a linear increase towards lower energies according to the probabilities of the corresponding interactions. The ability of X rays to penetrate material increases with energy; thus the lower-energy part of the spectrum is attentuated more strongly than the high-energy components as the X rays pass through an object. The low-energy components of the braking radiation have already been absorbed by the target itself and by the glass wall of the X-ray tube. An additional aluminum primary filter is used to absorb a large proportion of the soft X rays that would not appreciably penetrate the patient and hence would not contribute noticeably to image formation. Soft X rays result only in an unnecessary X-ray exposure.

The transmission of X rays through the body is approximately proportional to the third power of their energy. This characteristic leads to the phenomenon of beam hardening, that is, the beam becomes progressively more penetrating as it passes through the body due to selective absorption

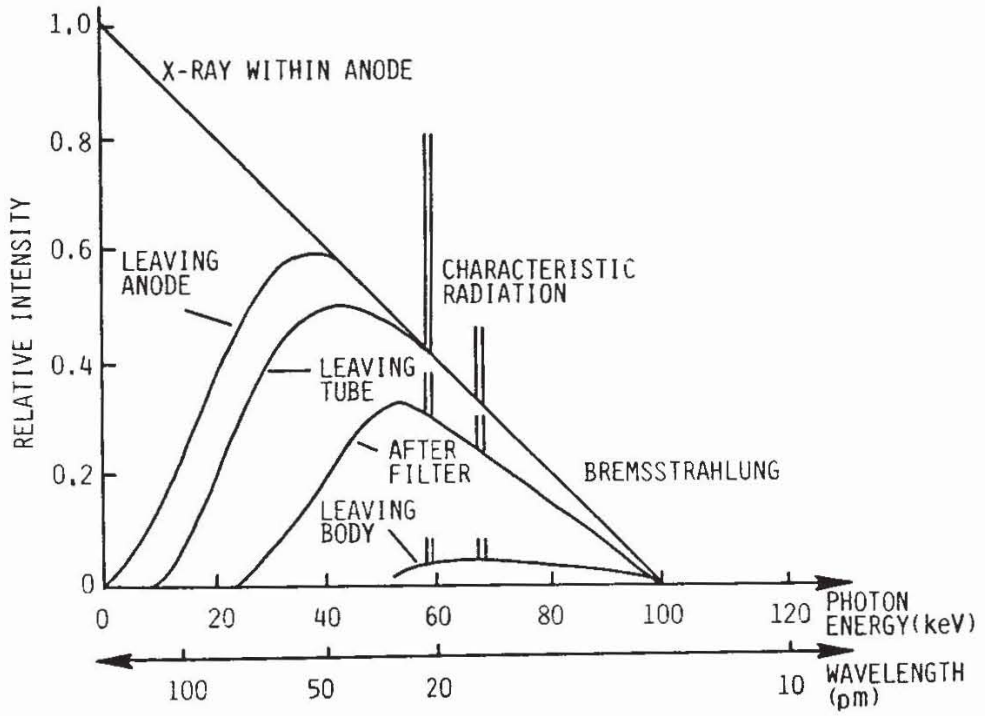


**Fig. 1.** Spectrum of X rays. Relative intensity versus photon energy and wavelength.

of soft X rays. The depth-dependent increase in the average energy of the polyenergetic beam causes image artifacts.

Biological damage occurs when ionizing radiation such as X rays penetrates tissue. The biological effects of ionizing radiation may be divided into two types: somatic and genetic. Somatic effects include minor reversible damage, such as reddening of the skin and loss of hair, but also include an increased risk of cancer and leukemia. Genetic effects are mutations in the reproductive cells that may affect later generations. A total body dose of 1000 rad is lethal for practically all vertebrates. Absorbed dose (expressed in rads) should be distinguished from exposure (measured in roentgens). The absorbed dose is not a direct measure of biological effect; for that purpose we define the dose equivalence (DE) measured in roentgen-equivalent-man units (rem). DE is related to the dose $D$ by the expression [23]

$$\mathrm{DE} = D \cdot \mathrm{QF} \tag{2}$$

where the DE and $D$ are measured in rads, and QF is a quality factor for the radiation in question. The QF has a value of 1 for 200-keV X rays, a value of 1.7 for low-energy electrons, and 30 for neutrons impinging on tissue. The QF does not distinguish among effects that depend on the type of cells; therefore an additional parameter, the relative biological effect (RBE), has been defined. Both the QF and the RBE relate the biological effects of radiation to the type of radiation. However, the RBE for a specific type of radiation is often different for various types of cells, whereas the QF is arbitrarily defined to be a constant for a given radiation. Tissues characterized by a high rate of cell division, such as bone marrow, lymph nodes, gonads (testicles and ovaries), intestinal mucous membranes, and skin, are highly radiosensitive. Because fetal tissues also fall into this category, X-ray examinations during pregnancy are contraindicated.

Federal laws restrict the amount of man-made radiation to which the public may be exposed (excluding medical X rays). Table I gives the recommended maximum permissible doses for the general public and radiation workers. The maximum permissible whole-body dose for radiological staff is 0.1 rad per week. The recommended upper limit for accumulated dose is $5(n - 18)$ rads, where $n$ is the age in years.

The exposure necessary to produce diagnostically useful X-ray images is difficult to ascertain with accuracy because it depends on the part of the body being imaged, the resolution and contrast required, and whether intensifying screens are used, as well as on the film and the radiologist. Typical amounts of radiation received by adults during particular procedures are given in Table II. The total amount of radiation depends on the number of views taken. The figures in the table can be contrasted with the typical dose for a CT scan, which is about 1.5–3 rad. For X rays the tissue

TABLE I

**Recommended Maximum Permissible Dose (MPD)**

| Type of exposure | MPD (rem/yr) |
|---|---|
| Radiation workers | |
| Whole body | 5 |
| Gonads or lenses of eyes | 5 |
| Skin of whole body | 30 |
| Hands and feet | 75 |
| Population | |
| Whole body | 0.5 |
| Gonads | 0.167 |

half-value layer (HVL) is about 2.5 cm, which means that for an average imaging procedure the absorbed dose in rems has a numerical value close to the exposure in roentgens. The dose from a CT scan is thus roughly equal to the amount of radiation received during a standard X-ray examination. In a continuous monitoring examination, such as during surgery, the dose can be an order of magnitude higher.

## *Attenuation of X-Rays* 2

A material-dependent fraction of X-ray photons penetrating matter interacts with particles of tissue or other matter being studied, resulting in the removal of these photons from the beam by absorption or scattering. The number of photons removed from the beam $\Delta N$ depends on the pathlength $\Delta x$, the total number of impinging photons $N$ and the material-dependent linear attenuation coefficient $\mu$

$$\Delta N = -\mu N \Delta x \tag{3}$$

TABLE II

**Radiation Quantities from Diagnostic X-Ray Procedures**

| Examination | Tube voltage/ anode current (kV/mA) | Entrance exposure (mR) | Mean marrow dose (mrad) | Gonadal dose (mrad) |
|---|---|---|---|---|
| Abdomen | 74/125 | 700 | 60 | 125 |
| Chest | 74/5 | 20 | 5 | <1 |
| Dental | 60/3 | 300 | 10 | <1 |
| Pelvis | 70/100 | 450 | 40 | 150 |
| Skull | 76/100 | 500 | 20 | <1 |

Putting this equation into its differential form and integrating gives the classical attenuation relationship:

$$N_{out} = N_{in} \exp(-\mu x) \tag{4}$$

where $N_{out}$ is the number of photons that remain in a beam, originally containing $N_{in}$ photons, that penetrates homogenous matter of thickness $x$. The same relationship holds for the remaining detectable intensity $I_d$ of a beam with incident intensity $I_0$ after penetration of the object:

$$I_d = I_0 \exp(-\mu x) \tag{5}$$

An inherent property of the human body, which makes X-ray imaging possible, is its spatially dependent attenuation coefficient; this results from the differing amounts of interaction between X rays and the various types of tissue. Thus the attenuation coefficient has to be expressed as a function of space and (because the attenuation of X rays by tissue is also dependent on photon energy) as a function of X-ray energy. For a fixed photon energy, the beam intensity detected in the $x$, $y$ plane $I_d$ $(x, y)$, after passing through matter parallel to the $z$-axis (see Fig. 2) is given by

$$I_d(E) = I_0(E) \exp\left[-\int \mu(x, y, z, E)\, dz\right] \tag{6}$$

Because imaging systems normally use polyenergetic sources, the detected beam intensity is obtained by integration over the whole spectrum of energies:

$$I_d = \int I_0(E) \exp\left[-\int \mu(x, y, z, E)\, dz\right] dE \tag{7}$$

Since effective attenuation of X rays is caused by the mass of penetrated material, attenuation for a specific material is often characterized by its mass attenuation coefficient $\mu/\rho$. By multiplication with the density $\rho$, the linear attenuation coefficient is obtained in units of inverse distance.

In the diagnostic range of X-ray energies (below 200 keV) three mechanisms dominate attenuation: coherent or Rayleigh scattering, photoelectric absorption, and Compton scattering.

Coherent scattering looks like the deflection of an X-ray photon by a target atom; but actually a photon exchange takes place. The arriving photon is absorbed by the atom, and its energy is spent to raise one electron to a higher energy level. This electron immediately returns from the unstable higher level to the ground state, reemitting the absorbed energy as an X ray of the same wavelength as the original photon. This interaction leaves the photon energy unaffected although the direction of

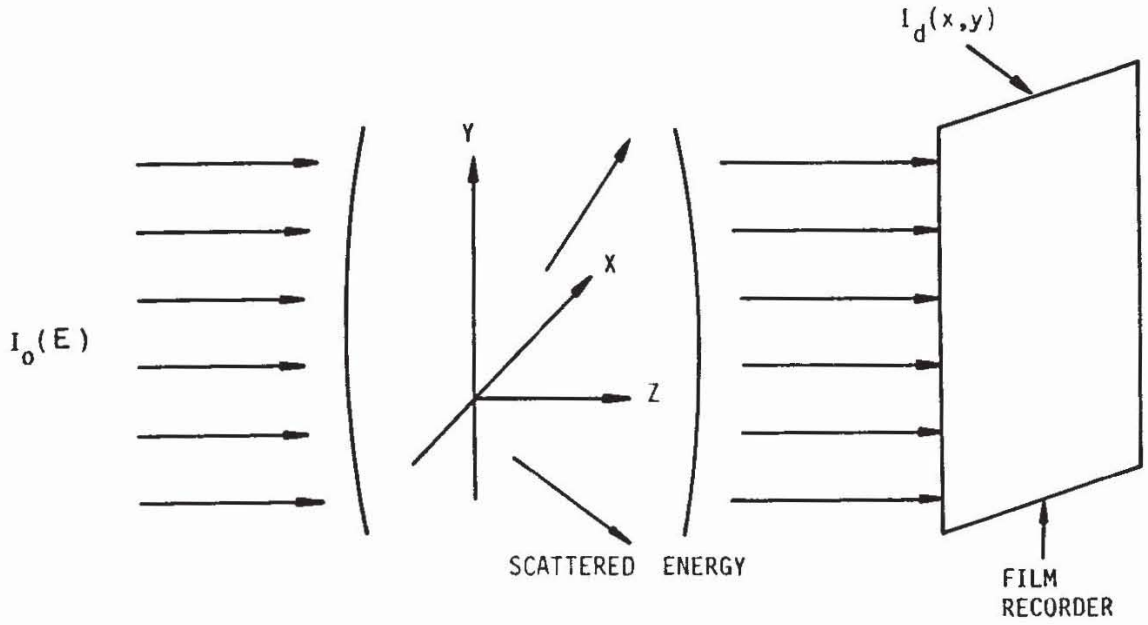


**Fig. 2.** Arrangement of X-ray system for attenuation consideration.

the beam may change. Of course, this scattering is limited to photon energies smaller than the K-shell ejection energy of the colliding atom. Since the maximum electron ejection energy is relatively small for the elements in biological tissue, this type of scattering is of minor importance in medical imaging systems.

Energy-dissipating photoelectric absorption removes photons from the X-ray beam and replaces them with lower energy photons, causing a shift in wavelength. Interaction between the impinging photon and the target atom consists of the ejection of a tightly bound electron. The excess kinetic energy of the electron is dissipated in the surrounding matter. The resulting vacancy is filled by an electron from the next larger shell, with emission of characteristic X-ray photons called fluorescent radiation. These photons have lower energy than the original photon. Lower-energy radiation is absorbed in the M- and L-shells and higher-energy radiation in the K-shell. Accordingly, the absorption spectrum shows sharp edges at the corresponding energies (Fig. 3b).

The linear attentuation coefficient due to photoelectric absorption increases approximately with the fourth power of the atomic number of the absorbing material, which is the reason for the strong attenuation of X rays by lead.

Compton scattering is the most important type of X-ray attenuation by tissue in the diagnostically relevant range of energy. It results from interactions between the X-ray photons and free or loosely bound electrons. A fraction of the photon energy is transferred by collision to an electron as kinetic energy. As a consequence of the photon's loss of energy, its wavelength becomes longer. Conservation of momentum

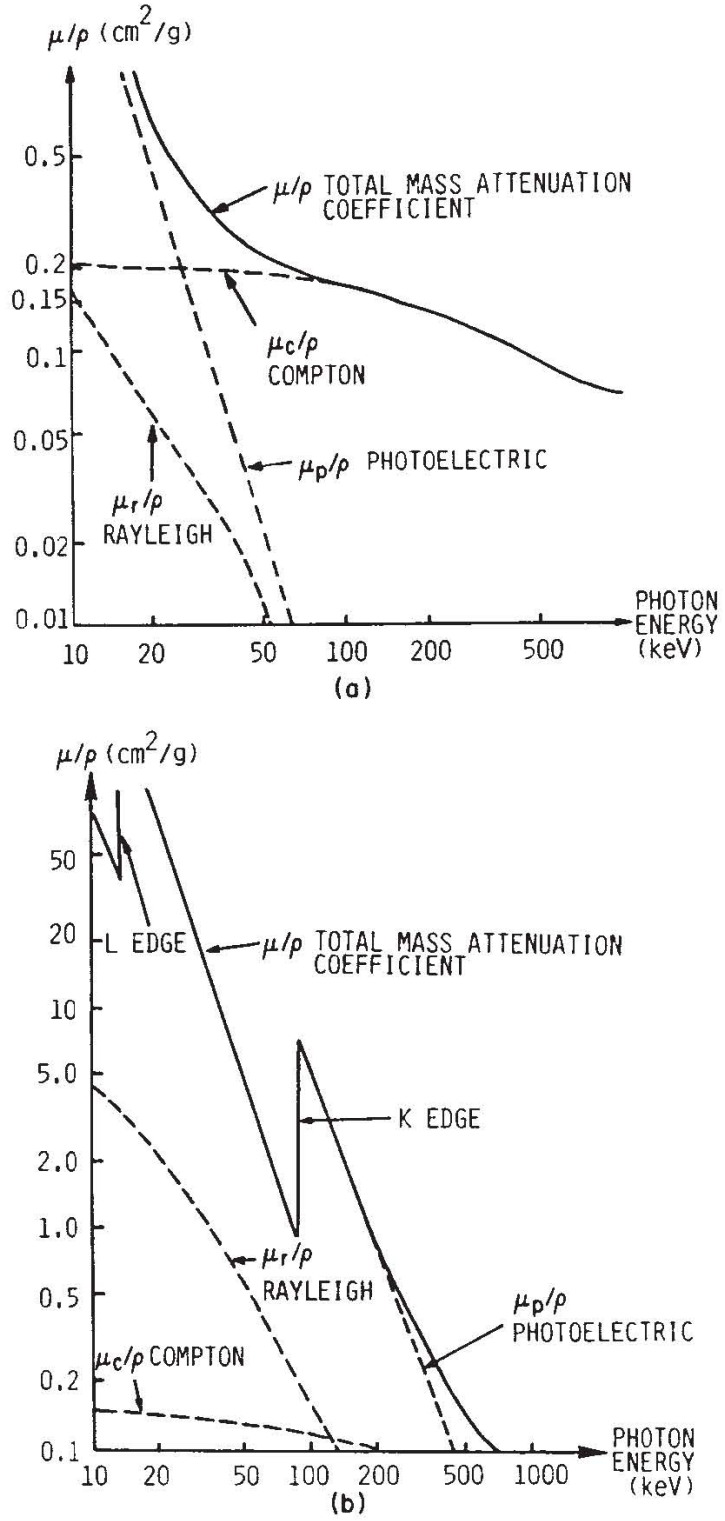


**Fig. 3.** Mass attenuation coefficient of (a) tissue and (b) lead.

results in a deflection of the X ray, whenever the electron is accelerated in a direction different from that of the impinging photon, the amount depending on the distance between electron and the undisturbed ray. Deflection is not restricted to the forward direction; backscattering can even occur. The energy range of diagnostic X rays is characterized by an

isotopic distribution of the scattering angle, whereas the effect of wavelength shift is very small (about 10% maximum); so the scattered X rays will also contribute to image formation, but of course only as severe artifacts.

Attenuation by these three modes of photon/tissue interaction adds linearly. The total attenuation coefficient is the sum of the three independent contributions:

$$\mu = \mu_R + \mu_P + \mu_C \tag{8}$$

R, P, and C refer to Rayleigh or coherent scattering, photoelectric absorption, and Compton scattering.

## *X-Ray Tubes* 3

X-ray tubes are essentially thermionic tube half-wave rectifiers run at very high anode voltages in the range 50–100 kV. Figure 4a depicts a static anode X-ray tube. The anode may be liquid cooled to prevent overheating if the tube is to be operated for extended periods. The apparent focal-spot size is smaller than the area of the tungsten target because of the chosen angle between target plane and the direction of the exit aperture of the valve. Figure 4b depicts a rotating anode X-ray tube. By using a rotating anode one can increase the effective heat dissipating area while keeping the radiating surface area small.

In diagnostic radiology, tungsten is commonly used as the anode material because of its high melting point (3370°C) and high atomic number ($Z = 74$). The probability for X-ray generating collisions of the impinging electron beam is proportional to the nuclear cross section target area, which is again proportional to the atomic number $Z$ of the target material. A second proportionality factor for the probability of X-ray emission is the energy of the impinging electrons; high energy either enables multiple radiating interactions to occur or provides the impinging electrons with enough energy to produce X rays even after energy-dissipating nonradiating interactions. Because the electron energy is proportional to the electron-accelerating voltage, the efficiency $\eta$ of the conversion of electron energy to X rays is given by

$$\eta = 1.4 \times 10^{-9}\, Z \cdot V \tag{9}$$

Thus for a tungsten target in an X-ray tube operated at 100 kV, the X-ray radiation efficiency is about 1%. The excess power of the electron beam must be dissipated from the anode as heat.

To generate X rays, the cathode filament is heated, and then high voltage is connected to anode and cathode. Electrons emitted from the heated cathode are accelerated towards the tungsten target anode. The

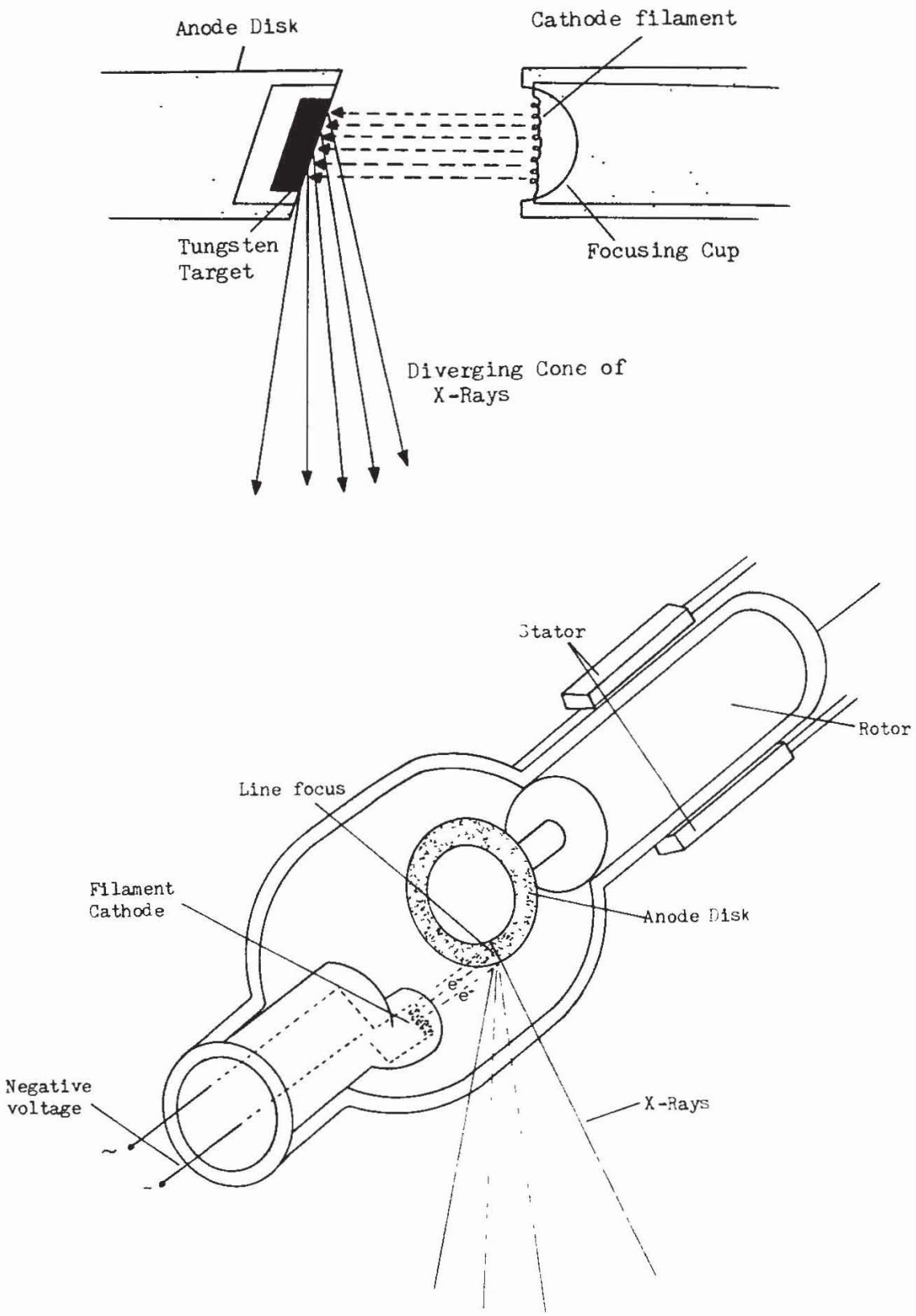


**Fig. 4.** Principal construction of X-ray tubes (a) static anode and (b) rotating anode.

upper energy limit of the bremsstrahlung is determined by the anode voltage. In terms of wavelength (in pm) it is given approximately by

$$\lambda_0 = \frac{1.24 \times 10^{-6}}{V} \tag{10}$$

Stationary anode X-ray guns operating in continous mode use accelerating voltages of 90–140 kV and anode currents in the range 10–40 mA. Pulsed operation, with anodes rotating at up to 10,000 rpm, permits higher electron beam densities, up to 600 mA, and hence greater tube output.

## *X-Ray Detectors* 4

X-ray detectors convert the invisible X-ray image pattern (i.e., the 2-D intensity-modulated X-ray field) that represents the projection of body attenuation coefficients into visible information: pictures. The characteristics of the detector are essential parameters of image quality, because they determine the obtainable resolution and contrast as well as the noise limits of the system. Three types of detectors are commonly used; these are based on the principles of photographic film exposure, fluorescent light conversion, and ionization pulse counting.

Fluorescent X-ray detection is the most important and most commonly used type of image conversion. Projection radiography is completely dominated by this technique. Some materials such as phosphorus or zinc cadmium sulfide are able to absorb the high energy of X-ray photons and convert it into a large number of lower-energy photons, in the energy range of visible light. This is done by multiple electron ejection and subsequent light emission by electron impact. Up to 1000 visible light photons can be produced by a single X-ray photon. X-ray projections can be viewed on a fluorescent screen; however, due to the low light intensity of the screen, pictures appear noisy and can be seen only in a darkened room.

Improvement of image quality is achieved by electronic light amplification using photomultiplier tubes. At present nearly all projection radiographic systems use X-ray image intensifier tubes, in which the fluoroscopic screen and the photomultiplier are combined in one enclosure. Figure 5 shows the construction of such a tube. The image intensifier tube contains a fluorescent screen, a photocathode, and a phosphor screen, all in an evacuated glass enclosure. X rays hitting the fluorescent screen are converted into visible-light photons. When these strike the photocathode mounted behind the screen, photoelectrons are emitted. The photoelectrons are then accelerated by a 25-kV potential and focused by an electrostatic lens onto a small phosphor screen. The image can be viewed via a television camera or a simple optical enlarging system. The use of the image intensifier tube typically results in a gain of 5000 over the use of a fluoroscopic screen alone.

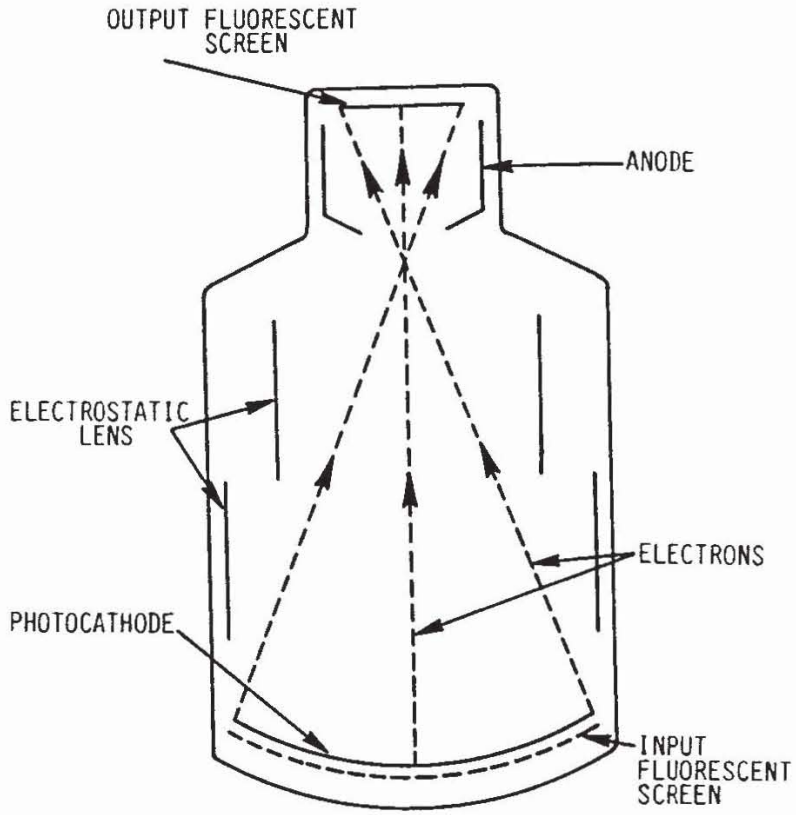


**Fig. 5.** Diagram of an X-ray image intensifier tube.

Radiographic film by itself is a relatively insensitive detector of X rays due to its low quantum capture efficiency. Increased sensitivity is achieved by providing emulsion layers on both sides of the film base and coating them with an intensifying screen of fluorescent material. X-ray conversion to visible light takes place in the fluorescent screen, the actual detector, and the emitted fluorescent light then irradiates the emulsion layer. Efficiency of producing grains on the film can thus be improved by a factor of about 1000.

Ionization chambers, mainly xenon gas tubes, convert X rays to electric current. X rays entering the detector tube cause ionization of the gas, thus increasing the current flowing between two electrodes maintained at a high voltage. Since the number of ions generated per X-ray photon is dependent on its energy, the detector current caused by a single photon is directly proportional to its energy. If more than one photon arrives at a time, the currents add linearly. The electrical signal can be converted to visible information in many ways, for example, on a TV monitor. In contrast to fluorescent screens, image intensifier tubes, and photographic image converters, the xenon gas detector cannot provide a whole picture but only one element of the picture. It is, however, like scintillation counters, able to perform energy selective measurements.

Scintillation counters consist of a radiation-absorbing medium in solid or liquid phase and a coupled photomultiplier tube (Fig.6). The most commonly used detector materials are thallium-activated sodium iodide

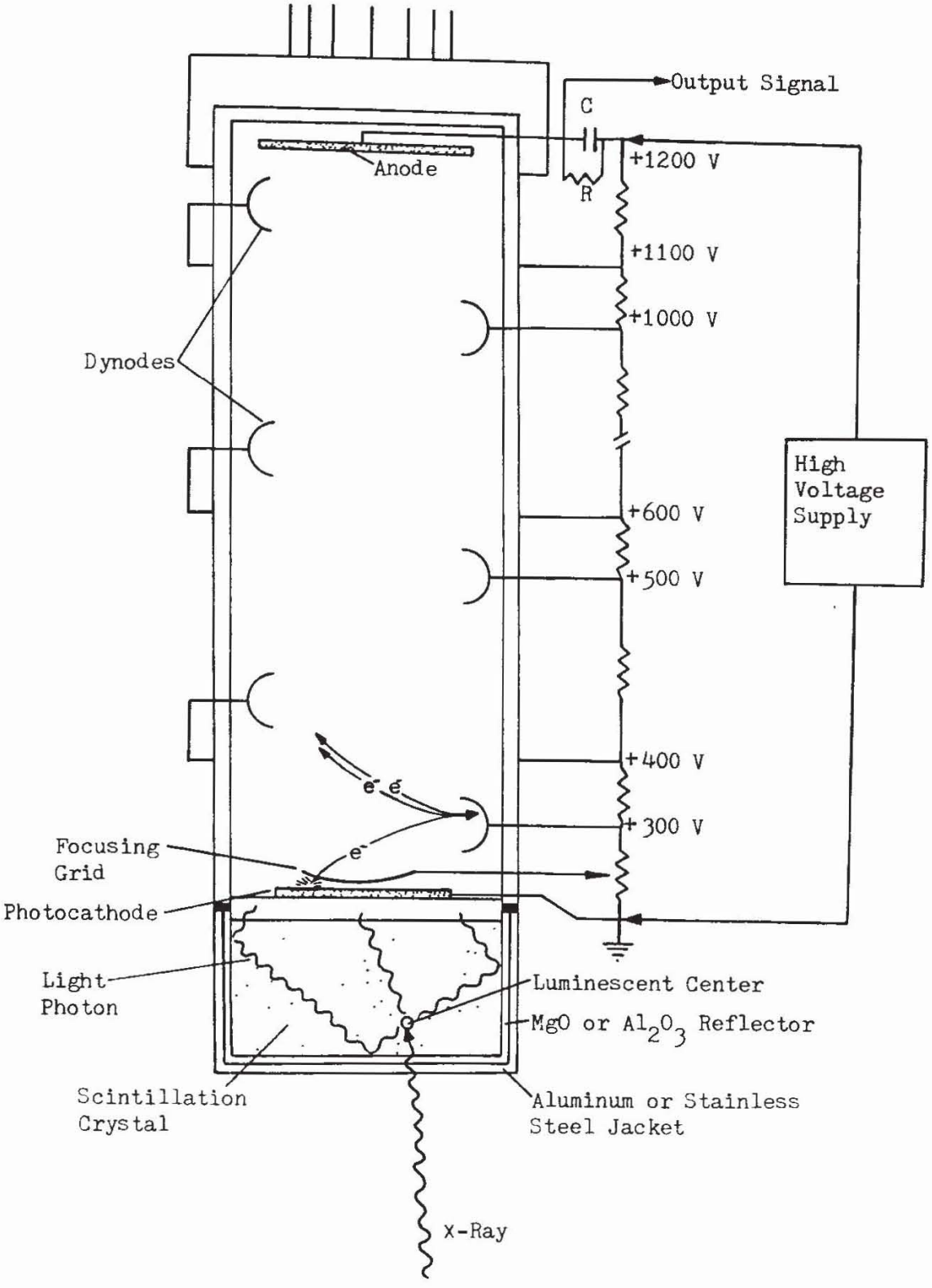


**Fig. 6.** Scintillation crystal detector with photomultiplier tube

crystals. Thallium enables the crystals to scintillate at room temperature. Impinging X-ray photons excite the NaI (Tl) crystals to luminiscence. The generated light ejects electrons from the photosensitive cathode of the photomultiplier; the electrons are then accelerated by an electric field and multiplied by secondary electron emission on the anode. Multiplication is

repeated in successive stages. This avalanche process produces an amplified tube current pulse that is proportional to the energy and/or number of incident X-ray photons. Due to the extreme sensitivity of NaI crystals to humidity, which converts the ionic iodine to molecular iodine, reducing its performance and increasing its sensitivity to temperature change (changes of more than 10°F per hour cause it to break) NaI is often replaced in newer systems by other materials even at the expense of conversion efficiency. Some commonly used materials are calcium fluoride, bismuth germanate, and cesium iodide crystals.

## B Projection Radiography

### 1 *Imaging of Projections*

The basic idea of projection radiography is the same as that of film projecting but without the use of optical lenses: A light source provides a homogeneous radiation field that is visualized on a screen. The object of interest is inserted between source and screen, the partial photon absorption by the object generates an intensity-modulated radiation field and, as consequence of linear ray propagation, a projection of the three-dimensional distribution of the absorption coefficients within the object becomes visible on the screen. Of course, projection always causes irreversible loss of information, because the distribution of the various absorption coefficients along a single beam is integrated and displayed as one value. Figure 7 shows the basic construction of projection radiographic systems.

The easiest way to describe the radiographic projection mathematically is to assume, for the first step, that due to its small focus the X-ray tube can be considered a point source of radiation. The output intensity after passing an object is described by the line integral of the attenuation

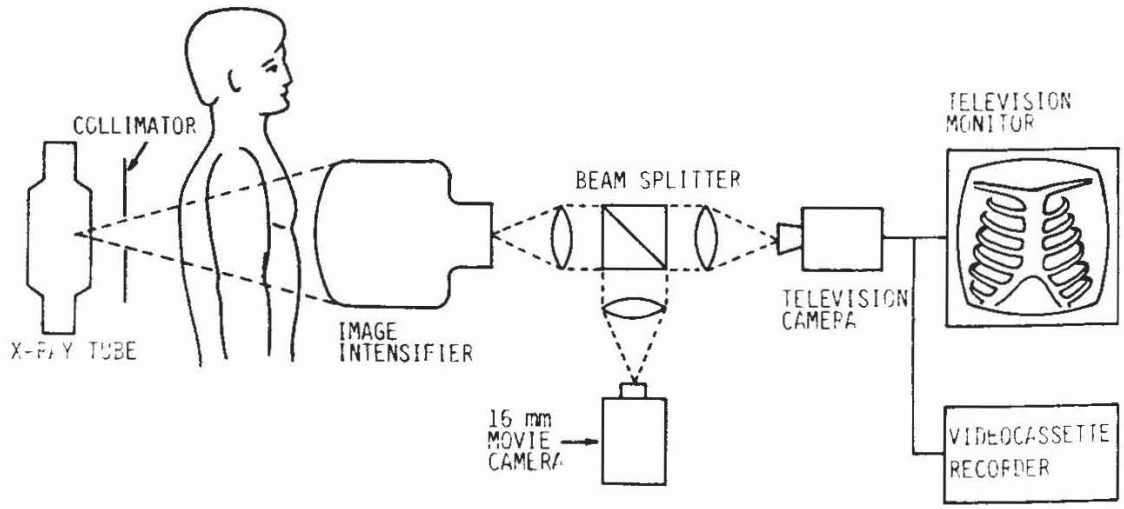


Fig. 7. Basic construction of a projection radiographic system.

coefficient $\mu(x, y, z)$ of the various rays. With the orientation of coordinates, source, and detector plane shown in Fig. 8, and restricting the calculation to a monoenergetic source, one can determine the detector plane intensity distribution $I_d(x_d, y_d)$ from

$$I_d(x_d, y_d) = I_i(x_d, y_d) \cdot \exp\left[-\int \mu_0(x, y, z)\, dr\right] \tag{11}$$

where $I_i(x_d, y_d)$ is the intensity of the detector plane in the absence of an object and $\mu_0$ the linear attenuation coefficient at the energy $E_0$. For a polyenergetic source the intensity has be to integrated over the energy:

$$I_d(x_d, y_d) = \int I_i(E) \exp\left[-\int \mu(x, y, z, E)\, dr\right] dE \tag{12}$$

As the intensity of spherical waves decreases with distance to the source and single points on a plane detector show different distances to the point source, a circular symmetric intensity falloff from the center to the corners is observed in the detector plane:

$$I_i(r_d) = I_0 \cos^3 \theta = I_0 \frac{1}{(1 + r_d^2/d^2)^{3/2}} \tag{13}$$

where $I_0$ is the intensity at the origin and $r_d = 0$.

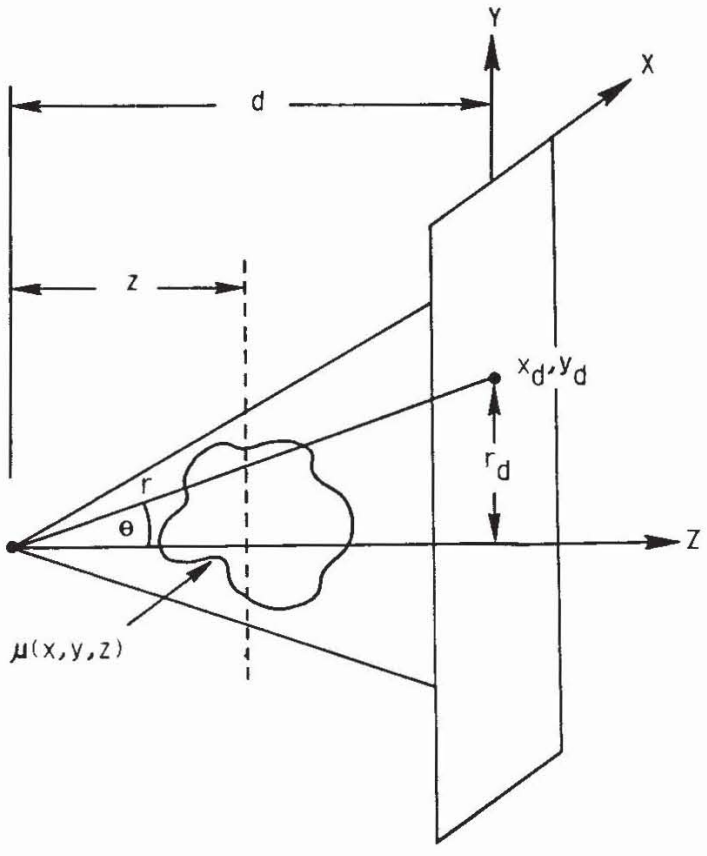


**Fig. 8.** Arrangement and coordinate orientation of a point source radiographic system.

As the X rays diverge with increasing distance from the point source, projections onto a spherical detector are magnified by a factor $M(z)$ equal to $d/d_o$, where $d$ is the distance between source and detector and $d_o$ the distance between source and object. This relation introduces a depth-dependent magnification factor. Parts of the object closer to the source show higher magnification than distant areas. Thus a depth-dependent distortion of the image is unavoidable.

Plane detectors show additional geometric distortion due to the obliquity of the screen against the X-ray wavefront, resulting in a magnification factor that is dependent not only on the depth of an object element but also on the distance of the picture element from the center of the screen.

When the intensity in the detector plane is expressed as a function of only the $z$-coordinate and the coordinate system $x_d$, $y_d$ of the detector plane, the distortion becomes apparent:

$$I_d(x_d, y_d) = I_i(r_d) \exp\left[-\sqrt{1 + \frac{r_d^2}{d^2}} \int_0^d \mu_0\left(\frac{x_d}{M(z)}, \frac{y_d}{M(z)}, z\right) dz\right] \quad (14)$$

where $M(z) = d/z$ specifies the depth-dependent magnification of the 2-D transmission function at plane $z$, and the radical is the obliquity factor due to the projection onto a plane.

Because real X-ray tubes always have a finite emission area, the point-source description of projection imaging has to be modified. Extended sources significantly affect the resolution of the detected image, which for point sources is theoretically limited only by the wavelength of the X-ray and, of course, by the resolution of the detector. Image formation of extended sources can be described either by spatial integration of elementary imaging equations obtained by decomposing the source area into single-point sources or by determination of the point response, specifying the image of a single-point transparent object. Normally, point response description is preferred since it corresponds to the experimental evaluation of the system's imaging equation and directly specifies important image quality parameters.

The point response of the system is expressed by its point transfer function which describes the image of a single point as a function of its location and the screen coordinates (Fig. 9). In contrast to point-source geometry, extended-source image formation is not a point-to-point projection. Instead, each object point is projected onto an area with source-dependent shape and intensity distribution. The image of a transparent point is the same as if the source were imaged through a disk diaphragm located in the object point within an opaque plane. The source is thus magnified by a factor of $m = (d - z)/z$, the ratio of the distances of the diaphragm from the detector and from the source. Extension of the point image results in overlap of neighboring point images, thus reducing

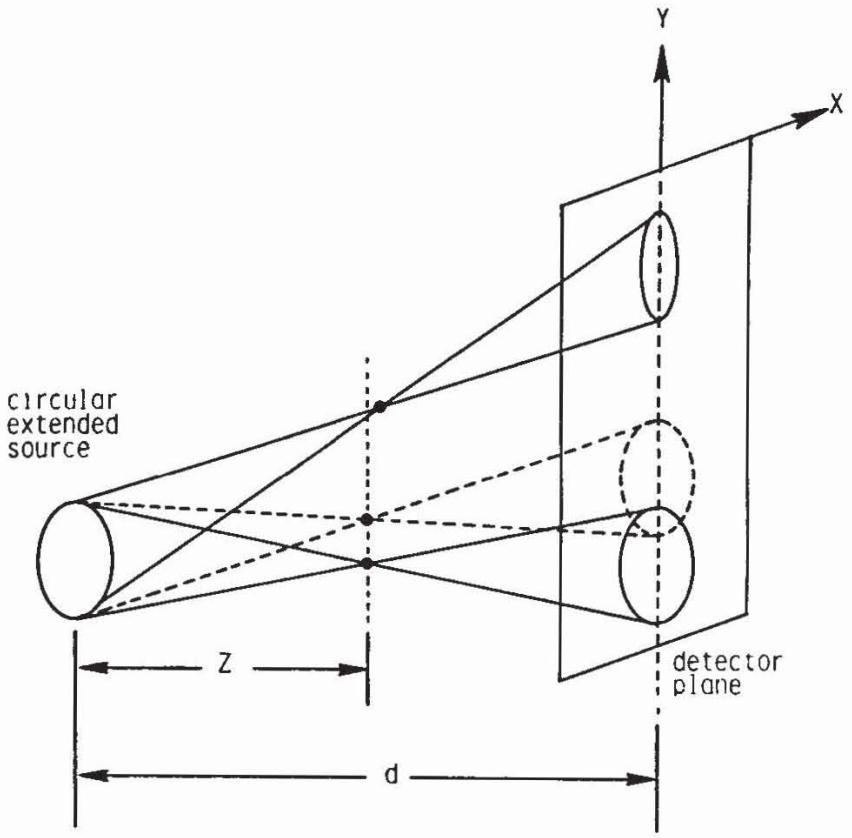


**Fig. 9.** Imaging characteristic of an extended source.

resolution, which is defined as the minimum distance between two points that can be imaged without overlap. Spatial extension of the point spread function (PSF) directly specifies the resolution. However, PSF and therefore the resolution are dependent on both the location of the object point and the position on the image screen. For $s(x_s, y_s)$ denoting the intensity distribution of a planar source, the PSF for a completely transparent volume element with the coordinates $x'$, $y'$, and $z$ is given by

$$h(x_d, y_d, x', y') = \frac{\eta}{m^2} \cdot s\left(\frac{x_d - Mx'}{m}, \frac{y_d - My'}{m}\right) \tag{15}$$

where $\eta$ is the collection efficiency that specifies the fraction of X rays passing the element. This equation for the PSF is derived by direct geometric projection with magnification $m$ and translation weighted by $M$. Intensity distribution on the screen due to an object section in the $x$, $y$ plane at $z$ with the 2-D transparency distribution $t(x', y')$ is obtained by the 2-D convolution of transparency and point spread function:

$$I_d(x_d, y_d) = \frac{1}{4\pi z^2 m^2 M^2}\, t\left(\frac{x_d}{M}, \frac{y_d}{M}\right) ** s\left(\frac{x_d}{m}, \frac{y_d}{m}\right) \tag{16}$$

where the obliquity of collection efficiency $\eta = \Omega/4\pi$ is neglected assuming that the solid angle $\Omega$ of the unit area in the object section is $1/z^2$ over the entire transparency.

The image blurring effect of source extension influences image quality similar to motion of the photographic film due to a small shift during exposure or motion of the object due to, for example, respiration or heart action.

## 2 Resolution and Noise

Considerations of the resolution of imaging systems include (1) the spatial dimensions of the smallest volume element (voxel) of an object that can be imaged without overlap and (2) noise, which primarily influences the intensity resolution of a single picture element (pixel) but also limits spatial resolution because of the need for sufficient image quality or contrast.

Spatial resolution of projection radiography is limited by the source area and geometry and by recorder characteristic. The main difficulty in detector design is to combine the two contradictory requirements of high resolution and high quantum capture efficiency, which directly influences the noise characteristics and specifies the fraction of impinging photons that contribute to image formation.

Noise, an unavoidable disturbance in any physical measurement, limits the attainable accuracy or resolution. Thus the ability to visualize anatomic structures is basically limited by the noise content of the measured signals. The crucial parameter, signal-to-noise ratio (SNR), is determined by the ratio of true image intensity variations to the random intensity variations of noise, which either result from statistical properties of the system or are introduced by independent additional noise sources such as, for example, thermal amplifier noise. The SNR of an image is a local parameter, defined as

$$\mathrm{SNR} = \frac{\Delta I}{\sigma_\mathrm{i}} \tag{17}$$

where $\Delta I$ is the intensity variation in the region of interest and $\sigma_\mathrm{i}$ the standard deviation of the background intensity (i.e., the rms value of intensity fluctuations of a blank image). Introducing the local contrast of an image as

$$C = \frac{\Delta I}{\bar{I}} \tag{18}$$

with $\bar{I}$ as the average intensity level, gives

$$\mathrm{SNR} = \frac{C\bar{I}}{\sigma_\mathrm{i}} \tag{19}$$

In X-ray imaging, the intensity of a pixel is given by the number of photons arriving within its area. The number of photons emitted by an

X-ray source in a given time interval varies according to a Poisson distribution [12]. Accordingly, emission of a mean of $N_0$ photons shows a standard deviation of $\sqrt{N_0}$. The same statistical distribution is valid for the projection image, the number of photons $N$ being given by multiplication with the transmittance $t$:

$$N = N_0 t \tag{20}$$

Thus, the SNR of an X-ray image is given by

$$\text{SNR} = C\sqrt{\phi ARt} \tag{21}$$

where $\phi$ is the photon density per roentgen, $t$ the transmission of the body, $A$ the area of a pixel, and $R$ the exposure of the body in roentgens. The basic conflict between spatial resolution, given by the pixel area $A$, and the X-ray exposure can be seen from this equation. High resolution and high SNR can be obtained together only with high patient exposure. Reduced exposure limits image quality, contrast, or resolution.

Interpretation of a picture, normally the evaluation of anatomic structures, must take account of the limited dynamic range of gray levels caused by low SNR. It usually makes no sense to attempt to extract information from an intensity variation (interpreting it as a structural detail) if the variation is smaller than the average intensity fluctuation due to noise. The situation can be improved by image processing methods such as, for example, a correlation analysis that improves SNR; but this does not affect the actual quality of the picture. Because the smallest useful intensity interval is equal to the mean noise amplitude, the number of differentiable grey levels in the picture is given by the ratio of maximum signal amplitude to rms noise.

A typical value for projection radiography image exposure is 50 mR, and transmission is about 5% for soft tissue. For a pixel size of $0.5 \times 0.5$ mm$^2$ and an X-ray density of $10^{10}$ photons/cm$^2$, corresponding to a photon density per roentgen of $10^{10}$ per cm$^2$, the SNR of the X-ray image pattern is about $250C$. With a contrast of $C = 0.1$, the SNR is about 25, corresponding to a limit of 25 gray levels in the picture. A further decrease of SNR is caused by incomplete screen conversion of X rays to visible light, reducing the effective light energy by the efficiency factor. Even if the conversion is performed with a gain in the number of photons, or electrons as in the photomultiplier tube, any conversion is combined with a loss of information since the conversion again represents a random process. SNR is scaled down by a factor of

$$\left(1 + \frac{1}{g}\right)^{-1/2} \tag{22}$$

where the gain $g$ is the number of photons produced by a single X-ray photon. If several conversion stages are involved (e.g., the series X-ray

photon, electron, and visible light photon of an image intensifier tube), then the degradation factor is, according to Macowksi (L 1),

$$\left(1 + \sum_{i=1}^{q} \frac{1}{\prod_{j=1}^{i} g_j}\right)^{-1/2} \tag{23}$$

where $q$ is the number of conversions and $g_j$ the gain of the single conversion. It can be seen that if the gain is high, the degradation is of minor importance. This may not be true for the loss of spatial resolution due to conversion.

Additive noise components that influence SNR are electronic amplifier noise and X-ray scatter. By adequate system design, amplifier noise can be reduced to a level that is neglible, if the photon intensity lies within a reasonable range. Scatter is a more serious problem since it is an inherent property of image formation as a component of X-ray attenuation. Compton scattering is the dominating attenuation mechanism, providing intensity modulation of transmitted beams by removing photons. The direction of some of the scattered photons lets them still reach the detector, but within a pixel other than that corresponding to their original beam; thus they represent additive noise. As a consequence, both contrast and SNR suffer reduction by a factor of

$$g_s = \left(1 + \frac{N_s}{N}\right)^{-1/2} \tag{24}$$

for the SNR and $g_s^2$ for the contrast, where $N$ is the number of transmitted photons and $N_s$ is the number of scattered photons, both per pixel. Typically the ratio $N_s/N$ is about 5, causing a SNR reduction by a factor of 2.5, which can be compensated by increasing exposure by a factor of 6. To avoid this additional X-ray dose, collimators or focused grids are used to limit detection to the direction of the transmitted beam (Fig. 10). Another way to reduce scatter noise is to use a single narrow pencil beam and a single detector system, recording the picture by successively scanning the single pixels.

The spatial resolution limitations of imaging imposed by recorder characteristics differ for the two types of image-forming system: a discrete pixel detector with a scanning pattern image and a whole-picture detector with no inherent image dissection.

For single pixel detectors, resolution is equal to the area of the detector. For whole-picture detectors (all based on visualization of X rays by fluorescent screens) resolution is dependent on screen thickness.

Excitation of luminiscence by an X ray results in light emission by the scintillation center corresponding to a point source of photons. With the coordinates given in Fig.11, the resulting intensity distribution on the film

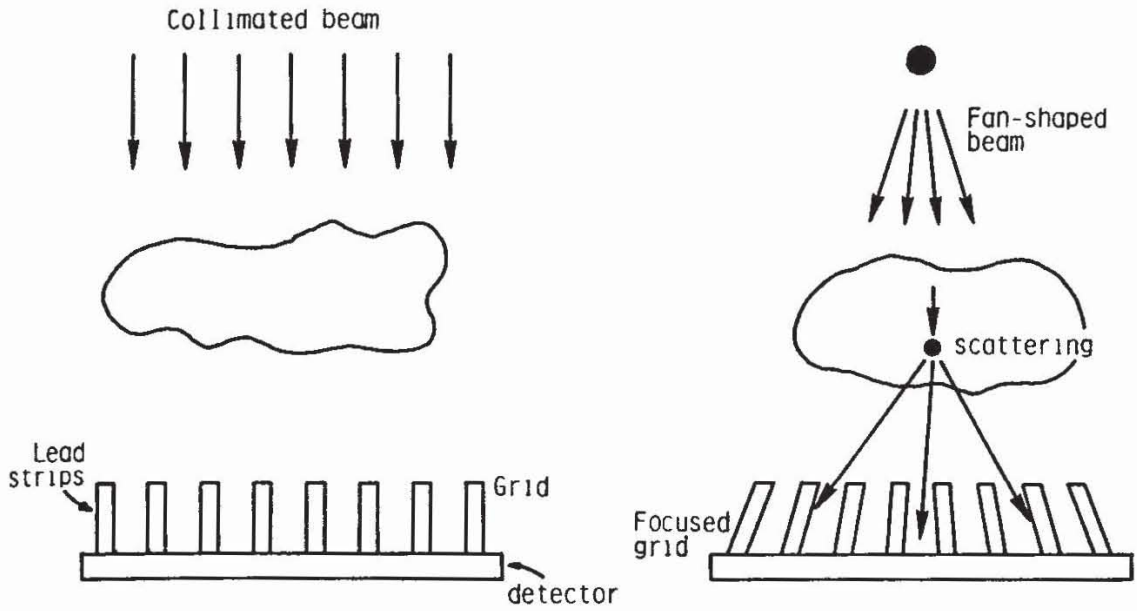


**Fig. 10.** Scatter-reducing grids for collimated parallel beam and fan-shaped beam.

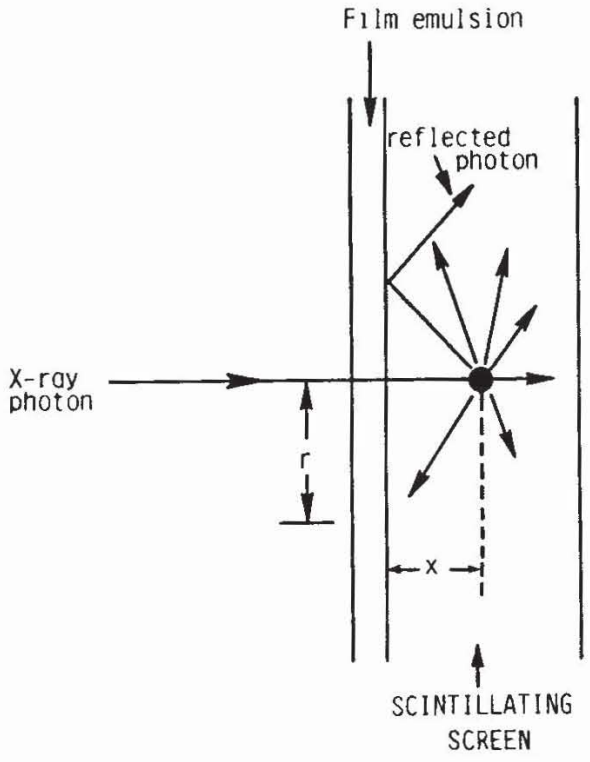


**Fig. 11.** X-Ray film detector with scintillation screen.

emulsion is

$$h(r) = K \cdot \frac{x}{(r^2 + x^2)^{3/2}} \tag{25}$$

where $K$ is a constant. This impulse response is infinite (i.e., there is no limitation of the irradiated area); however, suitable refractive indices for both film emulsion and screen limit the area in which light can enter the

film. Outside this area, which is dependent on the penetration depth $X_1$, light is reflected and does not contribute to the film exposure. Calculation of the impulse response or point spread function of an arbitrary X-ray photon must take into account the capture efficiency and depth distribution of scintillation centers. Resolution limits are defined using the corresponding modulation transfer function, namely, the spatial frequency at which the response drops to 10% of the maximum response. Double screen films have a spatial frequency limit of

$$f_1 \approx \frac{10\mu}{\pi\eta}\sqrt{1-\eta} \tag{26}$$

where $\mu$ is the linear attenuation coefficient and $\eta$ the conversion efficiency dependent on the screen thickness $d$. Typical values for radiographic films are $d = 0.25$ mm, $\mu = 15\ \text{cm}^{-1}$, and $\eta = 0.3$. The resulting bandlimit is 13 line pairs per millimeter, corresponding to a resolution of about 0.04 mm.

Figure 12 shows the modulation transfer function (MTF) for different recorder systems. It can be seen that photographic film offers the best resolution with a wide range of options for the resolution/efficiency tradeoff, depending on screen thickness.

Noise and resolution considerations for CT scanners are based on the same principles as for projection radiography; however, due to reconstruction from a multitude of projections and display of attenuation coefficients instead of intensities, the equations are slightly different. As an example, the SNR of a CT scanner using the reconstruction method of convolution

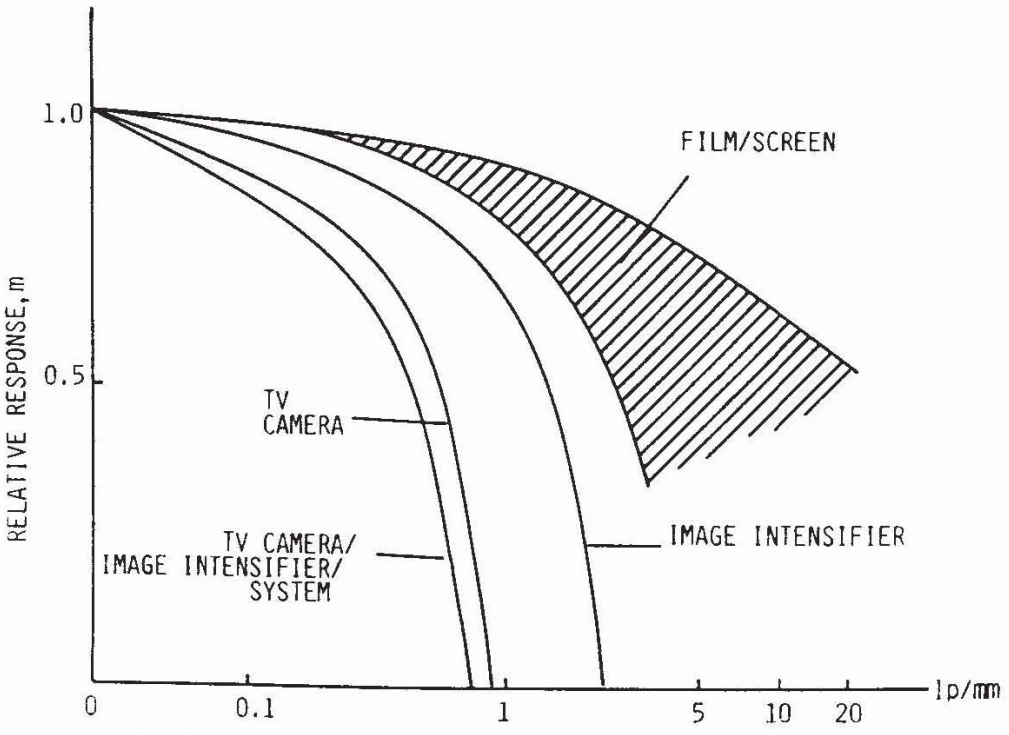


**Fig. 12.** Modulation transfer functions of different X-ray detectors.

backprojection is given by

$$\text{SNR} = KC\mu(N_m M)^{1/2} w \tag{27}$$

where $K$ is a constant dependent on the scanner MTF, $N_m$ the average number of photons per projection, $M$ the number of projections, $w$ the detector width, and $\mu$ the average attenuation coefficient. Resolution and SNR are again concurrent parameters, reduced detector width enabling higher resolution but at the cost of reduced SNR.

## *Projection Radiography Systems* 3

The conventional X-ray system consists of an X-ray tube, timer and control circuitry, X-ray filter, collimator, collimating grid, intensifying screens, and photographic film (Fig. 13). The patient is placed between the collimator and the grid. To avoid striping the picture with grid shadows, the grid is moved during exposure in the direction of the beams to spread the shadows equally over the picture area.

Direct viewing radiography systems have the same construction as the film systems, but the detector is replaced by a fluoroscopic screen or an image intensifier screen. Often detectors in a system can be exchanged to provide either photographic or direct viewing. Features of image intensifier systems include TV monitoring, simultaneous movie camera recording (as shown in Fig. 7), and electronic image storage. The main difference between TV monitoring and movie recording is the higher resolution of the photographic film. TV systems are limited to a resolution of about 500 lines, yielding a resolution of about 0.8 mm for 40-cm image format.

One of the main problems of projection radiography is the low contrast of the images due to the small differences in soft-tissue attenuation

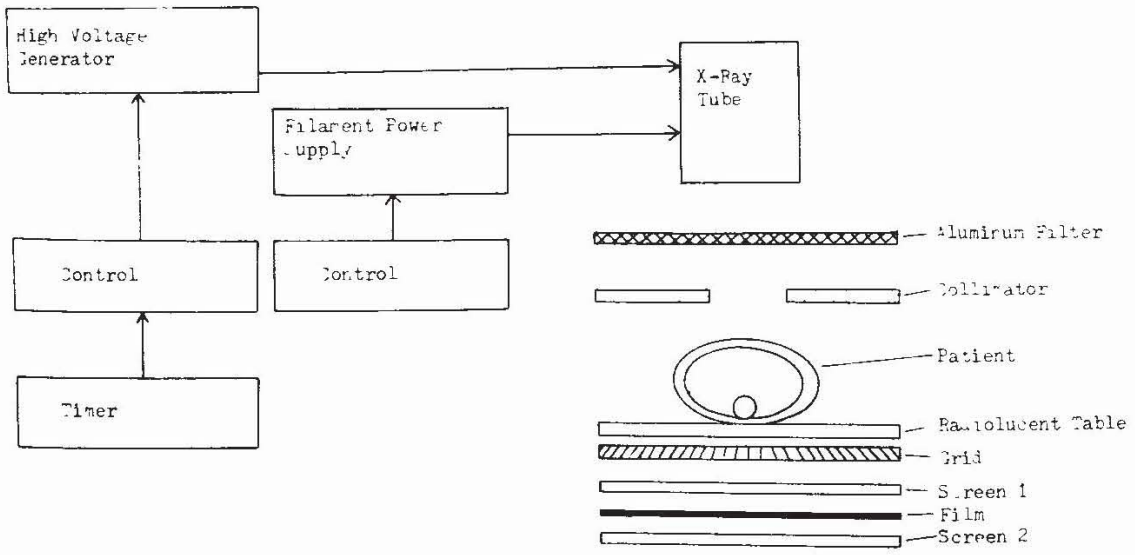


**Fig. 13.** Block diagram of conventional X-ray system.

coefficients, often less than 5% in the area of interest. In such cases, contrast enhancement is necessary to visualize structural details.

Image processing is an often-used procedure for contrast enhancement and structure detection. Spatial filtering such as high-pass filtering or differentiation increases contrast by removing unstructured background intensity; pattern detection algorithms are aimed at visualizing both known and unknown structures. Digital image processing is the most reliable and accurate technique used for contrast enhancing.

The contrast of many organs can be enhanced by administration of radiopaque dyes. A common application is swallowing of barium sulfate (insoluble and thus not absorbed from the intestine), which enables distinct visualization of its progress through the esophagus, stomach, and intestine. Movements of the organs can be studied. Absorption and excretion of other radiopaque dyes allow monitoring of structure and function of the kidneys and gallbladder, not only showing clear silhouettes of the urinary or bile passages but also indicating the efficiency of these systems by the excretion rate of the radiopaque substance. A most important diagnostic application of radiopaque dyes is angiography (i.e., the visualization of vessels and blood flow).

To remove unwanted structures from such contrast-enhanced projection images, digital subtraction radiography is applied. In this procedure a mask image is subtracted from subsequent images. If one of the pictures has been taken before the radiopaque dye has been administered, subtraction imaging provides improved contrast and elimination of unwanted image details coming from areas not under study. The main drawback of subtraction radiography, especially of subtraction angiography, is the large amount of motion artifacts. Less sensitive to motion distortions is energy subtraction radiography, in which two images are recorded in fast sequence using different energy spectra by switching the X-ray tube.

Contrast materials with distinctive K-edge absorption provide high contrast enhancement and background suppression.

## C X-Ray Computed Tomography (CT)

### 1 *CT Scanners*

Projection radiography suffers from the loss of depth information and the difficulties of detecting structural details that are partly hidden by overlying images of body areas that are not of interest. This problem is solved by selectively recording an image of a single plane in the body; the result is called a tomogram. An early technique of producing sectional views is motion tomography. By defined motions of the X-ray tube and the

film during exposure, images are produced in which all but one predetermined plane are blurred. Thus the projection shows a single plane with an added, approximately constant background intensity caused by the other planes. Contrast enhancement is not possible with this technique.

Computed tomography, by reconstructing axial cross-sectional views of the body by computation from a number of projections, provides significant improvement over motion tomography both in resolution and (especially) in contrast enhancement. The displayed view is usually oriented as if the patient's body were cut horizontally and the observer were looking at the cross section from below. The image represents the attenuation coefficients of small volume elements within the tissue slice. Differences of less than 0.5% can be detected.

The basic idea of computed tomography is to compensate for the inherent information loss of projection imaging by gathering additional data for the purpose of reconstructing depth resolution. This is done by successively recording projections in different directions. Thus a CT system operates basically in the same way as a conventional projection radiograph with the difference that the system has to be rotated around the patient and the image is computationally reconstructed prior to display. Various constructional solutions or CT scanners have been developed that are characterized by different source and detector systems, such as single pencil or fanned beams and single or array detectors, that require either translation–rotation or only rotational scanning. Source/detector layout and the resulting type of motion influence scanning time. A distinct evolution of system arrangements has taken place, each generation dominating the market for a time.

The first generation, typified by the original EMI Mark I head scanner, uses a single pencil X-ray beam and a single scintillation crystal combined with a photomultiplier tube as a detector. After one linear traversal of the X-ray tube and detector, which provides the projection along a single line divided into 160 discrete steps, the X-ray tube and detector are rotated; then another linear scan is recorded. The scan time is about 5 min.

Second-generation devices reduce scan time by employing ten detectors and ten pencil beams generated by adequate collimation of a single fan-shaped beam; the number of distinct recording positions is reduced by the factor of ten and scanning time to about 1 min.

The third generation eliminates the complex translational–rotational motion of the previous two generations. The X-ray tube, which produces a wide fan-shaped beam, and the spherical detector array rotate synchronously arond the patient. Scan times of about 5 sec and image reconstruction times of about 30 sec are possible.

Fourth-generation systems are similar to the third generation except that the detectors are arranged in a stationary ring around the patient and only

the X-ray source rotates (Fig. 14). Scan times can be reduced to as little as 1 sec, although reconstruction times are not significantly shorter than those of the third generation.

An imaging method based on X rays should ideally use as low an X-ray dose as possible. However, to resolve the small differences in X-ray attenuation between various soft tissues (approximately 0.5–5.0%) and to perform the scan in as short a time as possible it is desirable to use high-intensity X rays. The conflict is resolved by using low dose levels and detectors that feature high sensitivity and very low noise levels.

Generation I and II CAT scanners use scintillation crystal detectors coupled to photomultiplier tubes (PMT). The small number of detectors involved in these rotational–translational systems make it feasible from an engineering reliability point of view to use PMTs even though their construction makes them sensitive to vibration and the amount of wiring per detector is large.

The pure rotational scanning geometry of generation III virtually precludes the use of scintillation/PMT detectors. Instead, high-pressure xenon (Xe) gas tubes are used. A typical number of detectors is 512.

In generation-IV machines, with their stationary detector array, it is possible to return to scintillation detectors and either PMTs or solid-state photodiodes.

The computed pixels are arranged as rows and columns of a matrix. A typical matrix size is 512 × 512 pixels. Each of the image pixels corresponds to a small tissue volume element of a thickness between 1 and 13 mm and an area of 1 × 1 mm. The pixel brightness is proportional to the attenuation coefficient averaged over the volume element.

The linear attenuation coefficient is generally expressed as a decimal number. Because the human body is composed largely of water, an

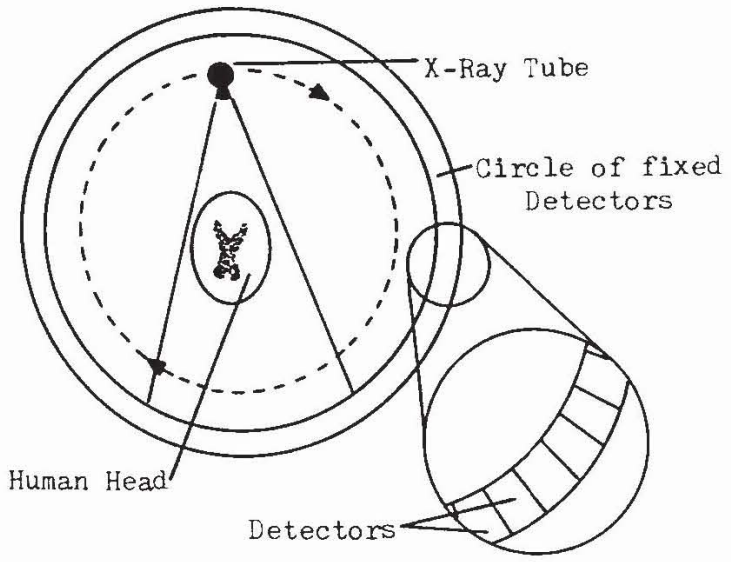


**Fig. 14.** Source–detector arrangement of fourth-generation CT scanners.

alternative way of presenting the data is as CT (or Hounsfield) numbers, which are defined by comparing the attenuation coefficient of the tissue under consideration to that of water:

$$\text{CT number (Hounsfield number)} = \frac{[\mu(\text{tissue}) - \mu(\text{water})] \times K}{\mu(\text{water})} \tag{28}$$

where $K$ is a scale factor set to either 500 or 1000.

CT scanners are capable of recording variations in X-ray attenuation of as little as 0.5%. To view such small differences, independent control of picture brightness and contrast is provided. The brightness (usually called window level) selects the mid-gray range for the image, whereas the contrast (called window width) sets the range of attenuation around the mid-gray level corresponding to peak black and white. Typical CT number ranges for various tissues are shown in Table III.

CT scanners are primarily limited to providing 2-D axial cross-sectional views. However, gathering a number of parallel projections enables the construction of arbitrarily oriented sectional views by rearranging the pixel values. Even 3-D imaging is feasible [13].

**TABLE III**

**Typical CT Numbers for Various Tissues**

| CT number scale | Tissue range | Specific material | Typical CT numbers |
|---|---|---|---|
| | | Metal clips, barium | >1000 |
| +1000 | | Dense bone | 1000 |
| + 900 | | | |
| + 800 | | Bone | 800 |
| + 700 | Bone | | |
| + 600 | | Calcified tissues | 600 |
| + 500 | | | |
| + 400 | | | |
| + 300 | | | |
| + 200 | | Blood clot | 40–60 |
| + 100 | | Soft tissue | 0–35 |
| Water 0 | Soft tissue | Blood | 0–12 |
| − 100 | | Fat | 0–100 |
| − 200 | | | |
| − 300 | | | |
| − 400 | | | |
| − 500 | Lung tissue | | |
| − 600 | | | |
| − 700 | | | |
| − 800 | | | |
| − 900 | | | |
| −1000 | | Air | −1000 |

### 2 *Medical Impact of X-Ray CT*

The main application of CT scanners is the diagnosis of abnormalities within the skull. Head scanning is used to detect causes of neurological disorders such as brain neoplasms, infarctions, cerebral edema, abscesses, intracranial hemorrhage, neurologic trauma, demyelinating diseases, and cerebral degenerative and opthalmologic diseases. Applications of CT body scanning include determination of the extent of malignomas; guidance of peritoneal biopsies of deep-seated abdominal and chest masses; management of osteoporosis; determination of the extent of mediastinal, pulmonary, hepatic, pancreatic, and renal masses; diagnosis of retroperitoneal disease; identification and localization of intraabdominal abscesses; determination in the anatomical pelvis, and some orthopedic examinations.

The use of CT body scanners is found to be inferior to other methods in areas such as dynamic studies of the circulatory and digestive systems, mammography, gynecology, and cardiology.

## III COMPUTED TOMOGRAPHY

## A Principles of CT

Various medical imaging techniques such as radiography, ultrasonic imaging, nuclear medicine imaging, and magnetic resonance imaging provide 2-D projections of anatomical structures and even metabolic processes. The inherent information loss of projection imaging, however, diminishes its diagnostic potential and impedes the interpretation of pictures. Because few possibilities exist for directly generating cross-sectional body views (e.g., in MRI or ultrasonic reflectivity scanning), there is considerable need for techniques aimed at computing true sectional views from projection data. Information loss of single projections is compensated by the recording of additional projections with different orientations [4–6,17,18].

Reconstruction of an object from its projections is a problem of linear algebra that can be solved in a straightforward manner by matrix inversion. Projection data in medical imaging, however, result in matrix sizes of $10^9$ to $10^{11}$ elements depending on resolution and image format; inversion requires computational efforts that cannot be mastered by available equipment. Simpler mathematical solutions to the problem are based on iterative reconstruction algorithms. Really practical solutions, however,

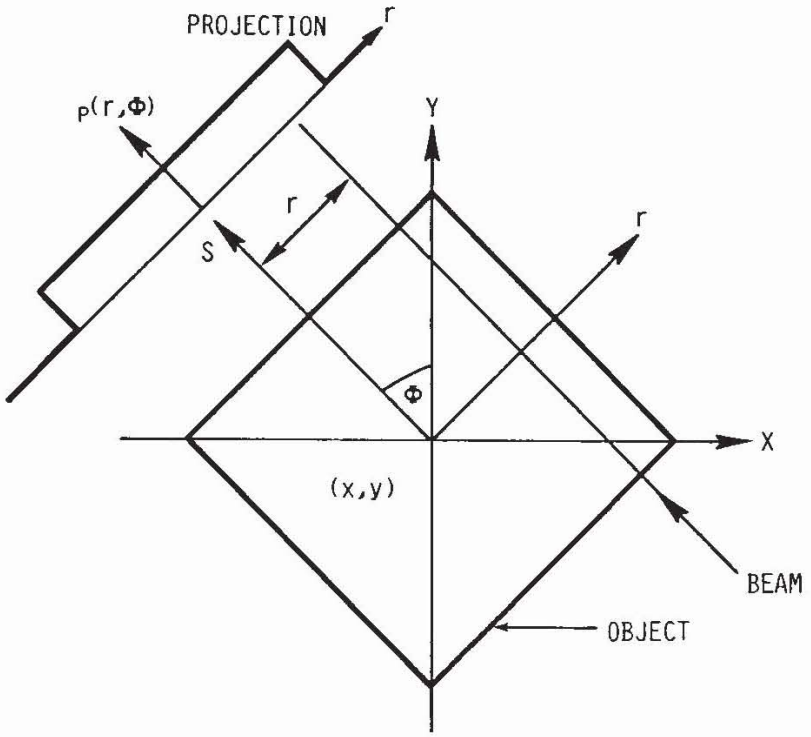


**Fig. 15.** Coordinate systems commonly used in CT-scanners.

are based on the Fourier transform approach, an analytical reconstruction technique.

The density distribution $a(x, y)$ to be reconstructed is described using $(x, y)$ coordinates as given in Fig. 15. In X-ray computed tomography $a(x, y)$ represents the linear attenuation coefficient $\mu\ (x, y)$; in nuclear medicine imaging it is the radioisotope density. The linear projections $p(r, \phi)$ are characterized by the angle $\phi$ of the contributing rays relative to the $(x, y)$ system. A single point with the coordinate $r_0$ on the projection with angle $\phi_0$ is given by the integration of the density function along the path $s$ of the ray with angle $\phi_0$ and the distance $r_0$ from the origin and is called the ray sum:

$$p(r_0, \phi_0) = \int_{r_0,\ \phi_0} a(x, y)\ ds \tag{29}$$

## Iterative Reconstruction B

The fundamental strategy of iterative reconstruction algorithms is to assume, as a first step, an arbitrary image and to compare the resulting computational projections with the actual recorded projection data. Corrections based on the discrepancies between these two sets of projections are applied to the image, attempting to match the projections. With appropriate correction algorithms, iterative reconstruction provides results corresponding to the true image up to a degree that is limited only by the

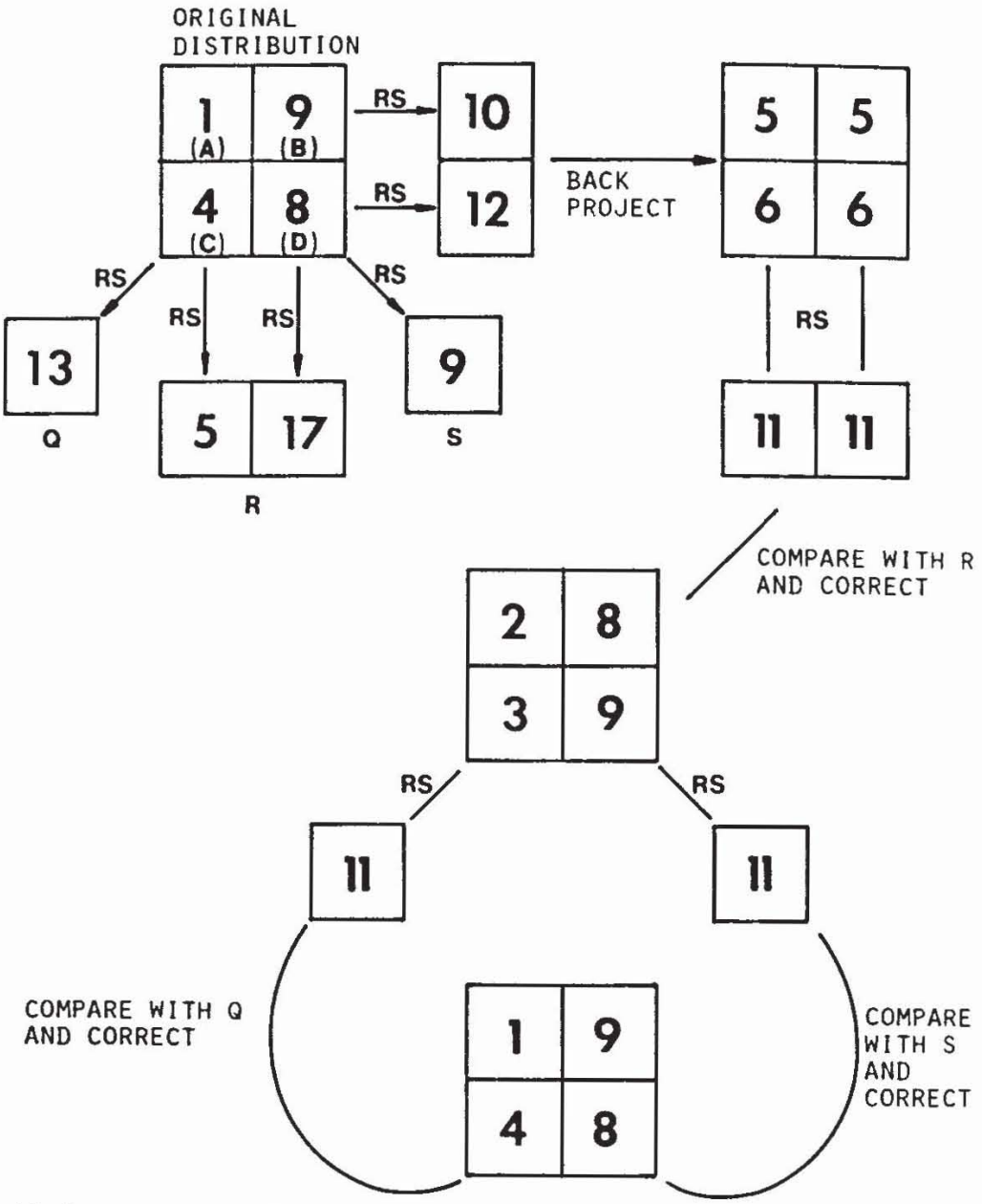


**Fig. 16.** Image reconstruction by algebraic reconstruction technique (ART). RS: ray sum.

number of iterations. Significant limitations of iterative methods are long computation times and possible lack of convergence due to signal disturbances. An example is given in Fig. 16, in which a consistent result is obtained after the second iteration.

## C Two-Dimensional Fourier Reconstruction

The 2-D Fourier transform $F_2$ maps the distribution function $a(x, y)$ onto the Fourier plane with the coordinate system $(k_x, k_y)$ as shown in Fig. 17:

$$F_2[a(x, y)] = A(k_x, k_y) \tag{30}$$

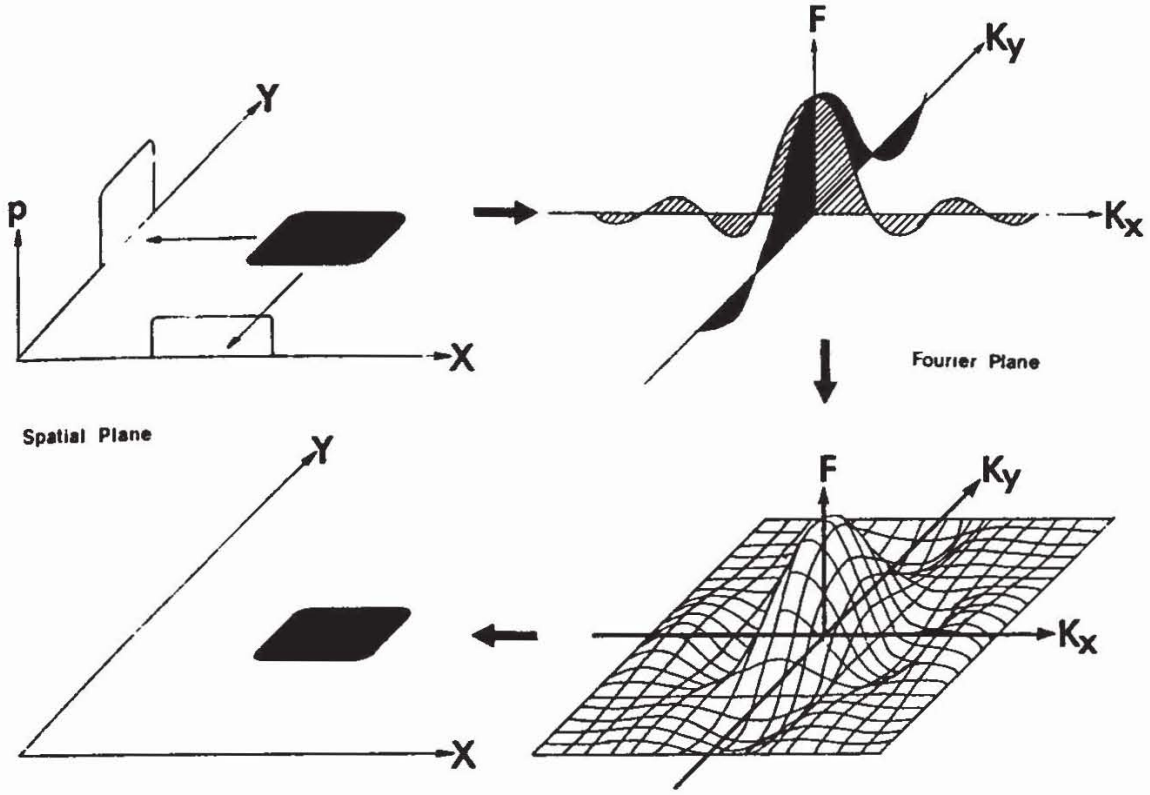


**Fig. 17.** Two-dimensional fourier reconstruction.

Performing a 1-D inverse Fourier transform of $A(k_x, k_y)$ along a radial section with an angle $\phi$ relative to the $k_y$ axis results, according to the central section theorem, in the projection of the distribution function under the same angle $\phi$:

$$F_{-1}[A(k, \phi] = p(r, \phi) \tag{31}$$

where $k^2 = k_x^2 + k_y^2$. Thus projections and distribution function are equivalent:

$$F_1[p(r, \phi)] = P(k, \phi) = A(k, \phi) \underset{\text{for all angles}}{\overset{\text{one central section}}{\Longleftrightarrow}} A(k_x, k_y) = F_2[a(x, y)] \tag{32}$$

The central point in this consideration is that the spectrum of the distribution function is equal to the spectrum of the whole ensemble of projections. Thus reconstruction of the density function can be performed by calculating the spectra of the collected projections filling the Fourier plane and the succeeding inverse Fourier transform of the resulting 2-D spectrum [9].

Some limitations, however, exist on the realization of this procedure. The number of recorded projections is limited, and as a consequence the 2-D spectrum of the distribution function is only a sampled version of the true continuous spectrum. In addition to this discretization, the spectra of the single projections are discrete Fourier series because they are calculated digitally by discrete Fourier transforms from the sampled projections.

So the spectrum of the distribution is represented by a finite array of Fourier coefficients. Reconstruction is possible only if the spectrum is band-limited and the density of coefficients is high enough to satisfy the sampling theorem. The upper band limit $k_u$ is directly coupled to the obtainable resolution of the reconstructed density function $w$ by

$$w = 1/2k_u \tag{33}$$

The specified resolution of the density function determines both the sample interval of the projections, which has to be equal to or smaller than the resolution, and the number $n$ of projections with equal angular distances, which is given by

$$n = \pi d/4w \tag{34}$$

where $d$ is the length of the projections or the maximum diameter of the object.

As an example, an object of diameter $d = 40$ cm requires, for a resolution of $1 \times 1$ mm of its density distribution, sampling of the projections in intervals of 1 mm and a total of 314 projections of equal angular distance over the range of 180°, that is, the angular increment of rotation is 0.57°.

Because the inverse 2-D Fourier transform normally is based on a rectangular matrix, and the Fourier coefficients that are obtained from projections do not fall into that matrix, interpolation is required as an intermediate stage of reconstruction. Table IV shows the total procedure of the 2-D Fourier reconstruction [10].

## D Backprojection

### 1 *Simple Backprojection*

The simplest attempt to reconstruct the distribution function $a(x, y)$ is to backproject the ray-sums onto the plane by assigning its value to all the points on the path of the ray (Fig. 18). Contributions from different rays to a single point are summed as follows:

$$a^*(x, y) = \sum_{j=1}^{n} p(x \cos \phi_j + y \sin \phi_j, \phi_j)\, \Delta\phi \tag{35}$$

with $r(x, y, \phi) = x \cos \phi + y \sin \phi$, where $\phi_j$ is the projection angle, $\Delta\phi$ the angular distance between projections, and $n$ the number of projections. Such an approximated distribution $a^*(x, y)$ is obtained with its relation to

**TABLE IV**

**Reconstruction Algorithms according to Brooks and Di Chiro [4]**

| Algorithm | Procedure | Number of multiplications[a] |
|---|---|---|
| Interative reconstruction (algebraic reconstruction technique) | Calculate all ray sums at a given angle | $2n^2$ |
| | Apply corrections to all points | $2n^2$ |
| | Repeat for all projection angles | $\times m$ |
| | per iteration: | $4mn^2$ |
| | (512 × 512 array): | $4.2 \times 10^8$ |
| Two-dimensional Fourier reconstruction | Take 1-D Fourier transform of projections | $mn \log_2 n$ |
| | Interpolate to provide a 2-D array of Fourier coefficients | $n^2$ |
| | Take inverse 2-D transform | $n^2 (\log_2 n)^2$ |
| | $(2.1 \times 10^7)$ | $\approx n^2(\log_2 n)^2$ |
| Fourier filtered back projection | Take Fourier transform of a projection | $2n \log_2 n$ |
| | Multiply each coefficient by $k$ | $2n(\log_2 n + 0.5)$ |
| | Backproject onto image plane using interpolation | $N$ |
| | Repeat for all projections | $\times m$ |
| | $(1.0 \times 10^8)$ | $mN$ |
| Convolution filtered back projection | Filter a projection | $0.5 n^2$ |
| | Back project | $N$ |
| | Repeat for all projections | $\times m$ |
| | $(1.6 \times 10^8)$ | $1.6 mN$ |

[a] $M$ is the number of ray-sums, $m$ the number of projections, $n$ the number of ray sums per projection, and $N$ the total number of picture elements. Numerical values are given for a 512 × 512 image array.

the true distribution function expressed by the spectra as

$$A^*(k_x, k_y) = A(k_x, k_y)/|k| = P(k, \phi)/|k| \tag{36}$$

The Fourier coefficients of the backprojected distribution differ from the true coefficients by a factor of $1/|k|$, which means division by the magnitude of the spatial frequency, resulting in a $1/r$ blurring of the image.

Since implementing backprojection is very easy, methods have been developed to compensate the $1/r$ blurring by proper filtering of the projections before they are backprojected. These filtered backprojection techniques perform the filtering either in the spatial frequency domain by Fourier filtering or in spatial domain by convolution filtering.

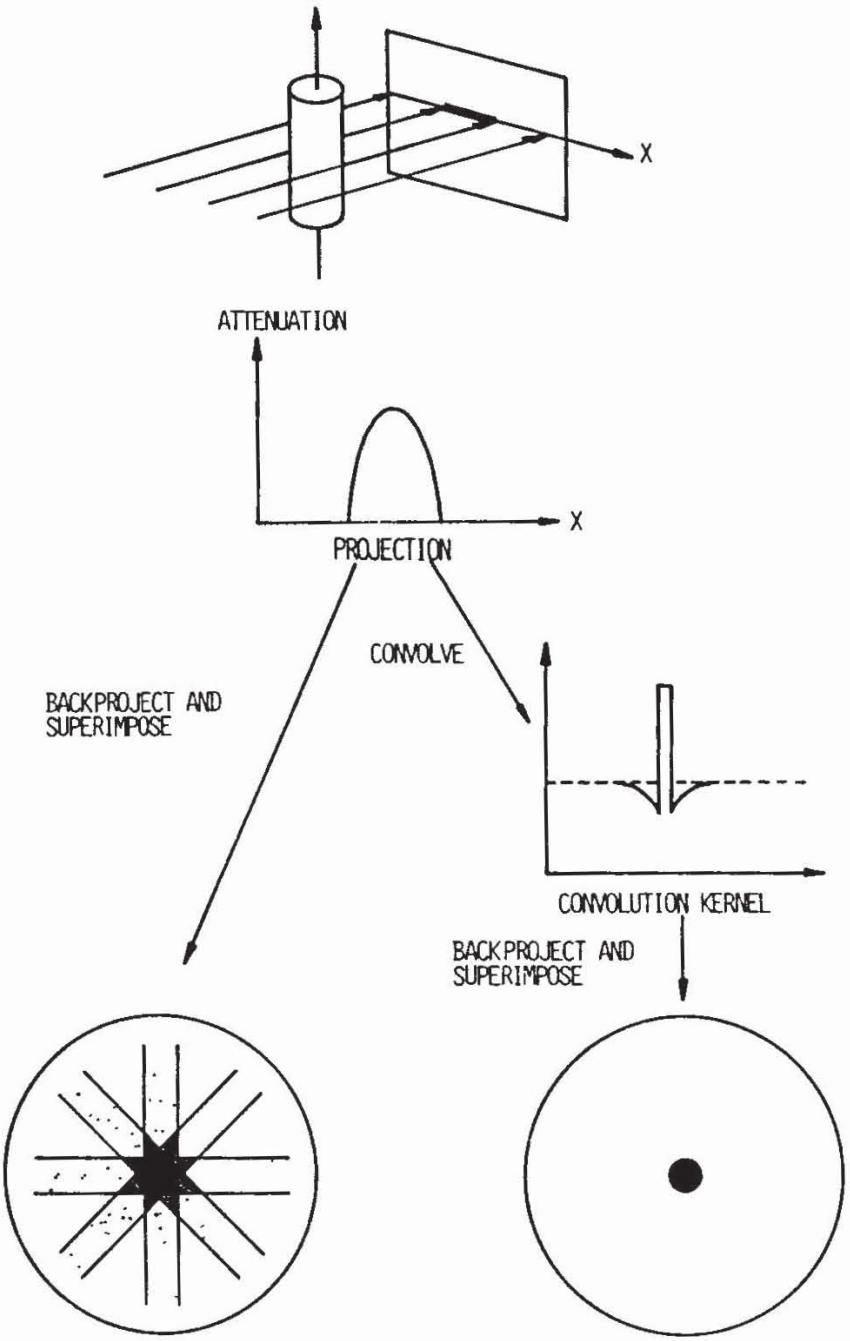


**Fig. 18.** Simple back projection and convolution-filtered back projection.

## 2 *Fourier-Filtered Backprojection*

Removing the $1/r$ blur of backprojection is done without time-consuming 2-D Fourier transforms by calculating the spectra of the projections using 1-D Fourier transforms, weighting the spectra with the factor $|k|$ (the filter transfer function), and then performing a 1-D inverse Fourier transform to obtain modified projections that are backprojected: this results in an undistorted image.

$$P(k, \phi) = F_1[p(r, \phi)] \tag{37}$$

Fourier filtering:

$$P^*(k, \phi) = P(k, \phi) \cdot |k| \qquad \text{for } -k_u < k < k_u \tag{38}$$

$$P^*(r, \phi) = F_{-1}[P^*(k, \phi)] \tag{39}$$

Backprojection:

$$a(x, y) = \sum_{j=1}^{n} p^*(x \cos \phi_j + y \sin \phi_j, \phi_j)\, \Delta\phi \tag{40}$$

## Convolution-Filtered Backprojection 3

Unlike spatial frequency domain filtering, convolution filtering removes the $1/r$ blur by space domain filtering of the projections [26]. Multiplication of two functions in the spatial frequency domain corresponds to the convolution ($*$) in the space domain; thus Fourier filtering,

$$P^*(k, \phi) = P(k, \phi) \cdot |k| \tag{41}$$

is equivalent to convolution filtering

$$p^*(r, \phi) = p(r, \phi) * F_{-1}[|k|] \tag{42}$$

The inverse Fourier transform of the filter transfer function $|k|$ is not defined because the function $|k|$ is not integrable. The divergence of the Fourier integral is, however, avoided by truncating $|k|$, resulting in a function that is equal to $|k|$ in the limits $|k| \leq k_u$ and to zero for $|k| > k_u$. This replacement does not influence the result of convolution filtering because $k_u$ specifies the upper band limit of the spectrum; so higher frequencies are not considered in any case, and Fourier filtering could also be done with the truncated transfer function. The impulse response of the convolution filter is thus given by

$$h(r) = F_{-1}[|k|_{\text{trunc}}] = k_u(2 \operatorname{sinc} 2k_u r - \operatorname{sinc}^2 k_u r) \tag{43}$$

A simple approach to this impulse response is obtained by considering the limiting case of $k_u \to \infty$, where $h(r)$ becomes an "impulsion" function containing a $1/r$ term as shown in Fig. 18.

The exact impulse response consists of a low-pass filter component given by the sinc function and an additive correction term. Both parts, however, suffer from the drawback that they are unlimited spatial functions and thus are not realizable. Simple truncation would affect the corresponding transfer function and remove the band limitation, increasing resolution but at the same time decreasing the SNR. Practical solutions have to find a compromise between SNR and resolution; they use low-pass filters with smooth rolloff characteristics to prevent overshoots and oscillations of the image intensity at sharp edges and some kind of approximation of the correction term to remove $1/r$ blur.

Convolution-filtered backprojection is used in nearly all commercial X-ray CT scanners. Various versions of convolution kernels are used for $1/r$ correction, most providing additional corrections for system-conditioned imaging errors. Table IV compares the various reconstruction algorithms and their necessary number of operations.

### E Nonlinearities

Reconstruction procedures are based on the assumption of a linear relationship between the measured projections and the line integrals of the desired distribution function. Both X-ray CT and radioisotopic imaging suffer from nonlinear effects. In emission tomography, undesired attenuation of gamma rays leads to different ray-sums of equal sources, depending on their distance from the detector and the distribution of attenuation coefficients between source and detector. As a result, central sources appear depressed. An approximate correction is made possible by averaging opposing projections.

Similar effects occur in X-ray CT due to beam hardening. Because X rays are always polyenergetic and attenuation is energy dependent, due to decreasing attenuation coefficients toward higher energies, low-energy photons are preferentially absorbed. Thus the mean energy of the beam progressively shifts to higher values. As a consequence, the effective attenuation coefficient of a single volume element is dependent on its location, leading to underestimation of attenuation coefficients in the central area of the image.

## IV NUCLEAR MEDICINE (GAMMA-RAY) IMAGING

Diagnostic imaging with high-energy electromagnetic radiation is based on two distinct principles: X-ray transmission imaging, which yields images of patient anatomy, and gamma-ray emission imaging, which reflects the function or metabolism of organs or other physiological systems. Emission imaging is achieved by selective administration of radioactive dyes so that the region under study emits gamma rays, which enables mapping of radioisotope distribution. The radioactive material is called a radiopharmaceutical and is administered to the patient by injection or inhalation. Radioactive labeling of characteristic metabolic compounds allows monitoring of specific physiological processes [8].

TABLE V

**Radionuclides Commonly Used in Nuclear Medicine**

| Radionuclide | Half-life | Transition | $E_{gamma}$ (MeV) | Production |
|---|---|---|---|---|
| Carbon-11 | 20.38 min | $\beta^+$ | 0.511 | Cyclotron |
| Fluorine-18 | 109.77 min | $\beta^+$ | 0.511 | Cyclotron |
| Phosphorus-32 | 14.29 days | $\beta^-$ | 0.695 | Reactor |
| Chromium-51 | 27.70 days | EC | 0.320 | Reactor |
| Cobalt-57 | 270.90 days | EC | — | Cyclotron |
| Gallium-67 | 78.26 hr | EC | — | Cyclotron |
| Molybdenum-99 | 66.00 hr | $\beta^-$ | — | Reactor |
| Technetium-99m | 6.02 hr | IT | 0.141 | Generator |
| Indium-111 | 2.83 days | EC | — | Cyclotron |
| Indium-113 | 100.00 min | IT | 0.393 | Cyclotron |
| Iodine-123 | 13.20 hr | EC | — | Cyclotron |
| Iodine-125 | 60.14 days | EC | 0.027 | Reactor |
| Iodine-131 | 8.04 days | $\beta^-$ | 0.364 | Reactor |
| Xenon-133 | 5.24 days | $\beta^-$ | 0.081 | Reactor |
| Thallium-201 | 3.04 days | EC | — | Cyclotron |

Classical nuclear medicine imaging, called planar imaging, generates 2-D projections of source densities. The drawbacks of projection imaging are avoided by tomographic systems that provide 2-D cross-sectional views or even 3-D imaging of radiopharmaceutical distributions by reconstruction from multiple projections [14,22]. Emission computed tomography (ECT) offers improved quantification and resolution compared with planar imaging. Collimation problems encountered in single-photon gamma-ray imaging are avoided by positron-emission imaging, in which collinear pairs of gamma rays are produced by positron annihilation.

X rays and gamma rays are, in their physical properties, the same type of electromagnetic waves; the difference is their origin. X rays are produced by high-energy electron bombardment of a target, whereas gamma rays are emitted by nuclear decay [25]. Emission or nuclear medicine imaging thus is not based on artificial radiation sources (in terms of technical instruments) but on radioactive materials, either naturally radioactive or artificially modified or excited to an unstable state, which results in nuclear decay and gamma-ray emission. An important characteristic of gamma rays is that they are monoenergetic, that is, they have a discrete spectrum with diagnostically used energies ranging between 50 and 700 keV (Table V).

Interaction of radiation with biological tissue, especially attenuation, is essentially the same for X rays and gamma rays. However, transmission imaging is based on these interactions with tissue, because attenuation is the information source for imaging anatomical structures, whereas in emission imaging (aimed at localizing the sources of radiation) attenuation is an undesired effect that decreases image quality.

# A Projection Imaging

## 1 Single Detector Scanning

The simplest technique of providing images of radioisotope densities is the single detector scanner. The detector (Fig. 19) embodies a single-hole collimator to ensure that gamma rays are detected from only one direction. The photons are converted to an electric signal that corresponds to the energy of the incident photons. Scanning the detector mechanically over the area of interest generates a 2-D projection of the source densities.

Since gamma-ray emission by radioisotopes is not directional but is uniformly spread over the whole space around the emitter, the small aperture of the single collimated detector results in the recording of very low photon densities. Therefore thick crystals have to be used to ensure an almost 100% quantum efficiency of the detector. Nevertheless the low density of incident photons leads to a rather poor SNR.

Due to the slow image formation of mechanical scanners, single detector systems are not suitable for dynamic imaging. An important application, however, is the static imaging of very large fields of view such as whole-body bone scans for detection of metastases.

## 2 Gamma-Ray Camera

Gamma cameras are basically an array of single detectors that enable imaging without mechanical scanning (Fig. 20). The components are similar to those in projection radiography, with the X-ray grids being replaced by a collimator. Scatter, however, excludes photographic film from being used as a detector/recorder combination. In radiography, grids reduce scatter effects substantially because their apertures are always

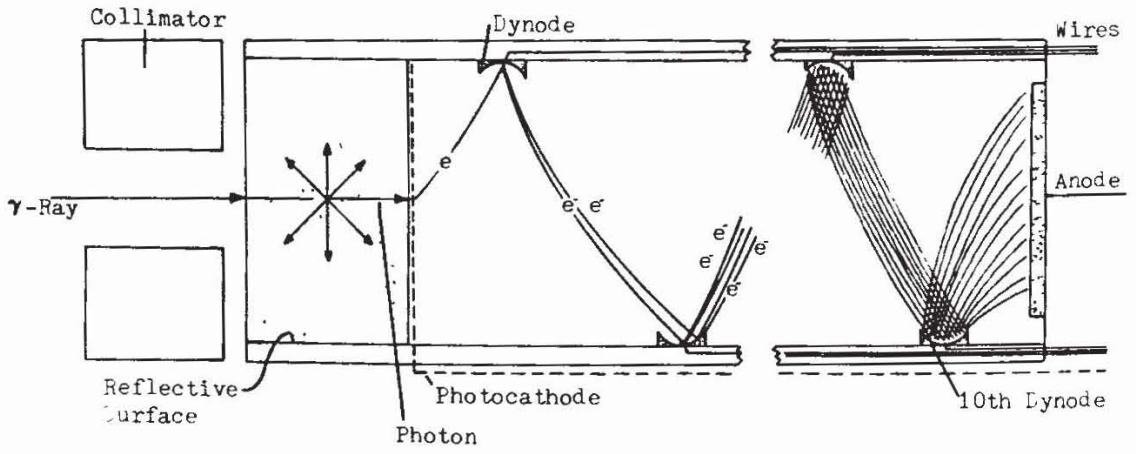


**Fig. 19.** Gamma-ray detector using single-hole collimator, scintillation crystal, and photomultiplier.

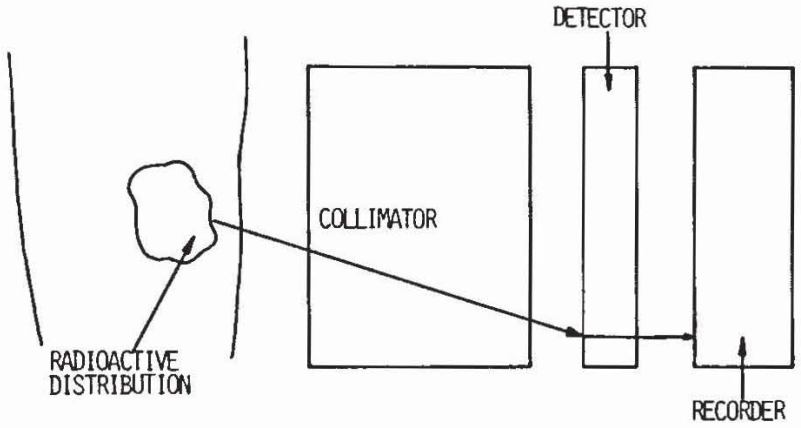


**Fig. 20.** Basic construction of gamma-ray camera.

directed towards the source; so, ideally, only unscattered photons reach the detector. Such a configuration is not realizable in gamma-ray cameras since the source location is not known in advance. However, the inherent property of gamma-ray sources of emitting monoenergetic radiation, unlike X-ray tubes, enables spectral separation of scattered and unscattered photons. Compton scattering, the only important scattering mechanism in the energy range of gamma rays, causes energy shifts large enough to be detected by an energy discriminating recorder (e.g., a photomultiplier). Since the number of light photons emitted by the scintillating crystal detector in response to a single gamma photon is proportional to the energy of the gamma photon, the pulse height of the PMT is also proportional to the energy. A pulse-height analyzer thus can exclude lower-energy scattered photons from contributing to image formation, as long as the incident photon rate is low and single events can be detected. As a consequence, gamma cameras use either PMTs or gaseous multiwire proportional counters as recorder elements. Resolution of the image is limited by the detector density, and SNR is determined by the number of recorded photons.

### *Anger Camera* 3

Resolution of the gamma camera can be improved, without increasing the density of recorders, by implementing a continuous whole-image detector screen. The divergent light beams that are emitted by a single scintillation event are sampled by several discrete recorders, and the location of the light source is calculated from the intensity distribution. Thus, still using discrete detectors, resolution becomes (within reasonable limits) independent from detector density. Principle and block diagram are shown in Fig. 21. The position of the gamma-ray incidence $(x', y')$ is calculated by weighting the single detected intensities or the numbers of photons $n_i$ by the coorinates $(x_i, y_i)$ of the PMTs [7,15].

$$x' = \sum_i x_i n_i \Big/ \sum_i n_i \tag{44}$$

$$y' = \sum_i y_i n_i \Big/ \sum_i n_i \tag{45}$$

The gamma-ray energy is determined by summation over all recorders.

The resolution of the Anger camera, named after its inventor, depends on the accuracy of coordinate determination which is mainly limited by photon emission statistics. Various formulas exist for improving resolution by better adaptation to photon statistics than the above mentioned weighting formula. Current solutions provide a resolution of typically 0.2 cm for an array size of 40 cm (i.e., about 40,000 pixels) using 25 photomultipliers.

## B Single-Photon Emission Computed Tomography (SPECT)

Since the advent of positron emission tomography (PET), which uses the advantages of photon pair emission and thus shows some special constructional features, computed tomography based on other types of nuclear decay with only one emitted photon is called SPECT.

SPECT scanners are based on a rotating gamma camera, usually an Anger camera, that provides projection data for the reconstruction of 2-D sectional views or 3-D images of source distribution. Reconstructional

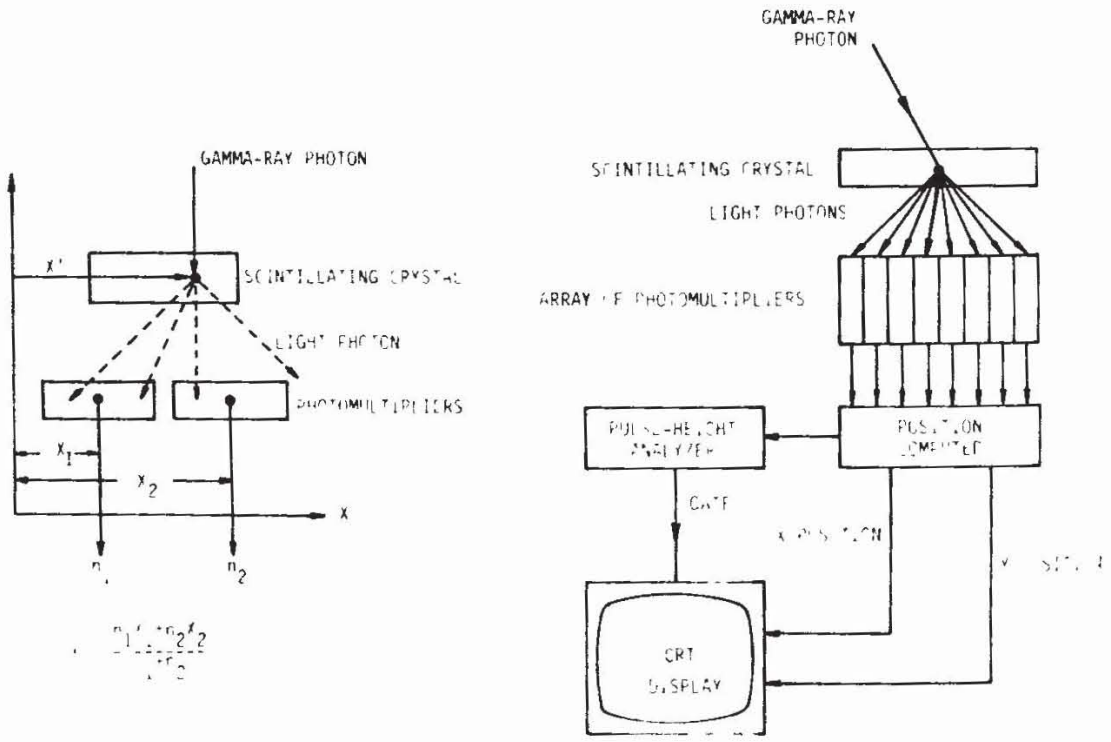


Fig. 21. Basic concept and block diagram of Anger camera.

algorithms are exactly the same as those used in X-ray CT and described in Section III. Usually, convolution-filtered backprojection is used.

Unavoidable attenuation losses of gamma rays, resulting in image distortions, are corrected by assuming a homogeneous distribution of a fixed-value attenuation coefficient, or for better accuracy they are compensated on the basis of actually measured values of the attenuation coefficients. For this purpose an external gamma-ray source is used to generate a transmission CT that provides the attenuation coefficients of the body.

An Anger camera does not restrict the projections to a single line as to X-ray CT cameras. It gives complete 2-D projections; thus, not only can a single cross section be reconstructed, but a whole set of parallel sections is obtained from the available data. This enables 3-D imaging as well as reconstruction of arbitrarily oriented sectional views by rearrangement of pixels.

## Positron Emission Tomography (PET) C

The main problem of radioisotopic imaging is the lack of an inherent imaging structure. This deficiency is removed in SPECT by a collimator that defines the direction of the beams that contribute to a single pixel. Positron emission provides a much easier way to define the direction of a projection. Because in positron annihilation two photons are emitted in opposite directions, coincidence detection of both photons defines the beam direction as the connecting line between the two detectors, thus excluding noncoinciding photons from contributing to image formation [27]. This technique is called electronic collimation. Physical collimators are necessary only to shield the detectors against radiation from out-of-plane positron emission. However, detectors must be located on opposite sides of the patient.

The lack of individual detector collimators increases detector aperture and facilitates the construction of tomographic scanners, because the rotation of the projection plane can be achieved without mechanical movement. Consider the ring detector in Fig. 22. Counting all coincident photon pairs that reach any two given detectors in the ring determines the ray-sum of the beam that is defined by the connecting line of the two detectors. The ensemble of all ray-sums from the same direction gives the projection of the source distribution for the given angle $\Phi$. Coincidence measurements with a different set of detector pairs then provides the projection for another angle. Thus a complete set of projections is obtained that corresponds to data recorded in X-ray tomography; so the same reconstruction techniques are used to generate the sectional views of radioisotope distribution.

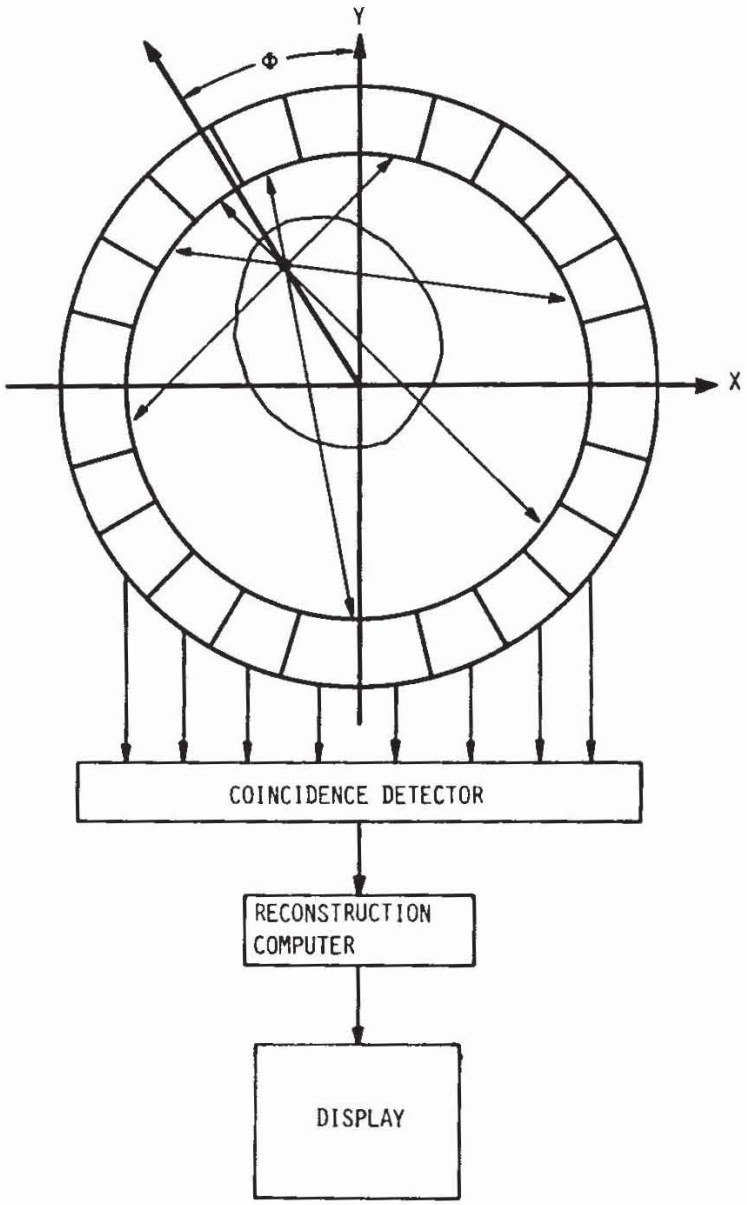


**Fig. 22.** Ring detector used in PET.

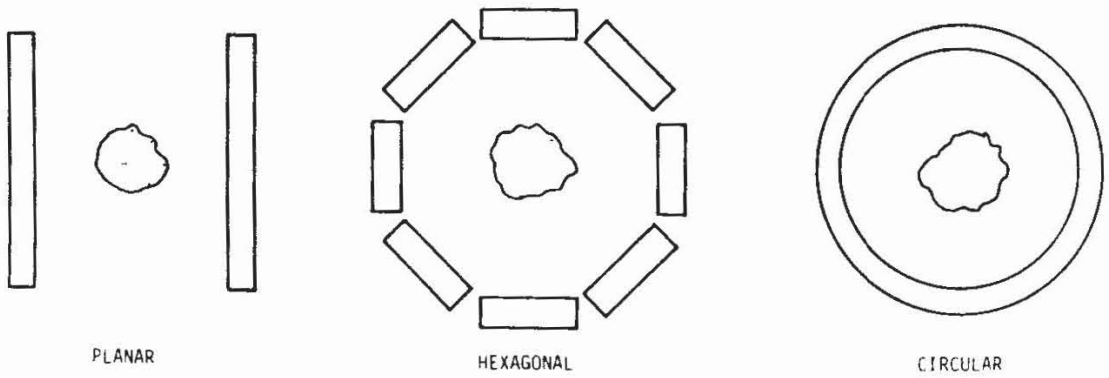


**Fig. 23.** PET detector arrangements.

All projections are measured concurrently by recording all arriving photon pairs and summing the events to the corresponding ray-sums. Simpler detector arrangements, such as the planar and polygonal detector types shown in Fig. 23, have to be rotated around the patient to collect a complete set of projections. The number of projections, determining spatial resolution, depends either on the angular resolution of the system rotation or on the number of detectors in the positron ring detector.

A major source of noise in PET is random coincidences. These arise by chance when two uncorrelated photons are detected nearly simultaneously and recorded as coincident events. The frequency of these random coincident events increases with the random single counting rates in each detector and with the coincidence resolving time (the maximum time interval allowed between two events that are considered coincident). The noise can be reduced by decreasing the coincidence resolving time. However, there are practical limitations on how much this time can be reduced, since it is determined by several factors including variations in the time of flight, the time needed to form a light pulse in the crystal, the response time of the PMT, and the resolving time of the electronic circuitry beyond the PMT. In scintillation detectors the resolving time is in the range 0.5–30 nsec.

Unfortunately, whereas the frequency of random coincidences increases as the product of the single events recorded in each detector, the true coincidence rate increases only linearly with the count rate. In a typical PET system, the number of coincidence events identified by a pair of detectors is less than 1% of the number of single events recorded by each detector.

A block diagram of a coincidence counter is shown in Fig. 24. The signals from the two detectors are amplified and low-pass filtered (LPF) to remove high-frequency noise. An amplitude threshold circuit rejects low amplitude signals and produces an output pulse when a high-energy signal is detected, as from a gamma ray resulting from positron annihilation. The pulses are fed to an AND gate that produces an output pulse only when both inputs are high. The coincidence pulse is stored as a count for that particular pair of detectors and is used for image formation.

Spatial resolution of PET has two inherent limitations: (1) the two annihilation photons are not precisely collinear because of the positron and electron momentum, and (2) the positrons travel variable distances from the radionuclide before annihilation. The distance is a function of the positron's kinetic energy and the electron density of the tissue. The combined effects of these factors result in a fundamental uncertainty of the radionuclide location of about 2–3 mm. In present systems, however, resolution is limited to about 0.5 cm due to position detection in accuracy, photon statistics, and sampling.

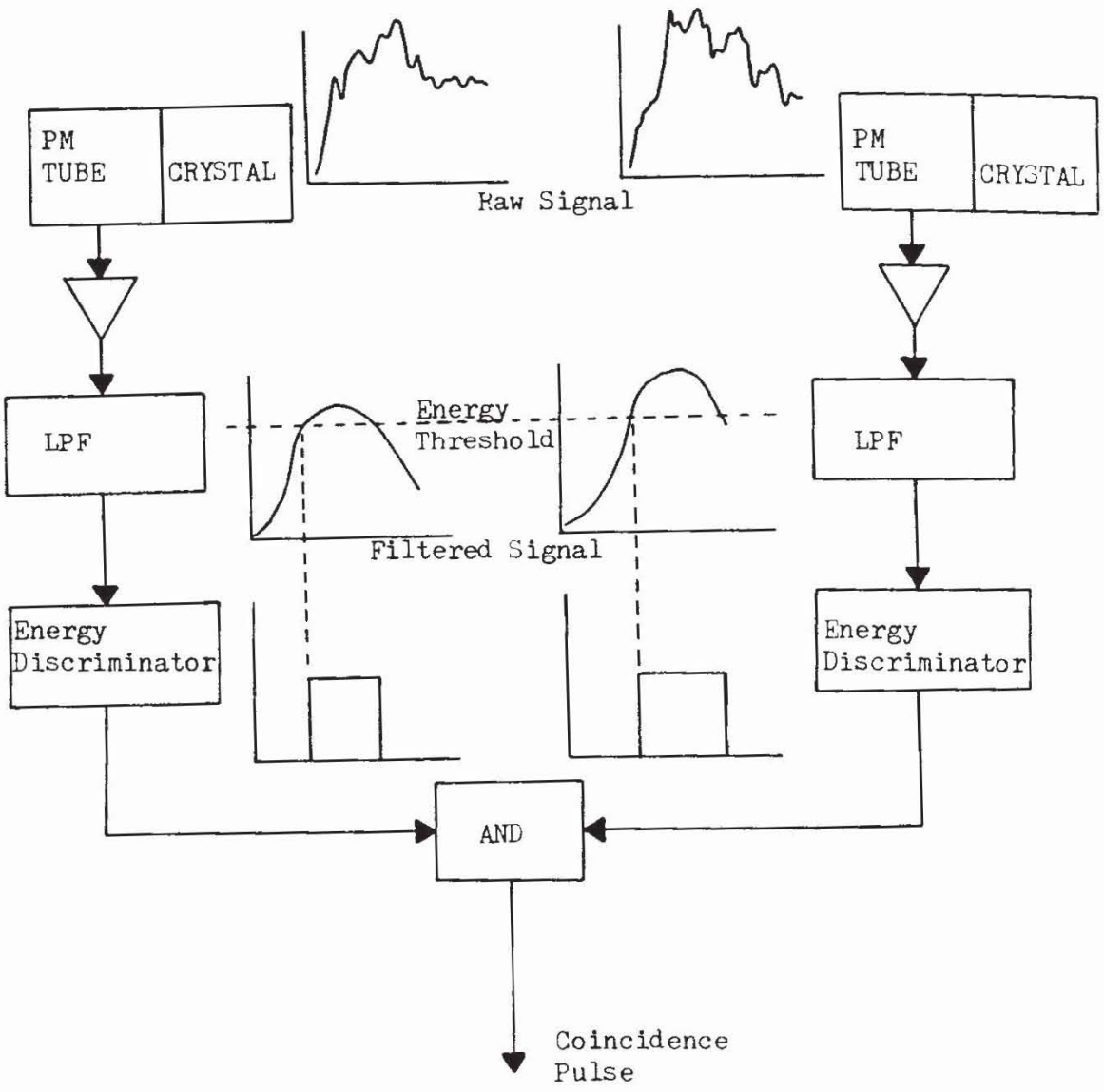


**Fig. 24.** Detection arrangement for coincidence counting.

## D Radionuclides

Unstable nuclides, called radionuclides or radioisotopes, decay spontaneously (i.e., without external stimulation) to some stable state. Both naturally occurring and artificially produced radionuclides are used in nuclear medicine. Basic characteristics of radioisotopes are average life or half-life, mode of decay, and nature of emission. Half-lives (i.e., the time within which the mass of the radionuclide reduces to half its original value due to decay of diagnostically used elements) range between 270 days and 2 minutes (Table V). Transition energy can be released by emission of alpha, beta, and/or gamma radiation. The suitability of a radioisotope for nuclear medicine imaging depends on several factors: (1) It has to emit gamma rays or positrons, (2) it has to be available in a chemical form convenient for administration, and (3) the chemical form has to be physiologically

TABLE VI

**Frequently Used Procedures in Nuclear Medicine**[a]

| Procedure | Radionuclides | Chemical forms |
|---|---|---|
| Plasma/blood volume estimation | $^{125}I$, $^{131}I$ | Radioiodinated serum albumin |
| Red cell mass and life estimates | $^{51}Cr$ | Labeled red blood cells |
| Vitamin $B_{12}$ absorption | $^{57}Co$ | Labeled cyanocobalamin |
| Thyroid function test | $^{123}I$, $^{131}I$ | Sodium iodide |
| Tumor and abscess imaging | $^{67}Ga$ | Citrated complex |
| Thrombus imaging | $^{111}In$ | Labeled platelets via oxine |
| Cerebrospinal fluid imaging | $^{111}In$ | Chelated complex with DTPA |
| Myocardial imaging | $^{201}Tl$ | Thallous chloride |
| Cardiac blood pool imaging | $^{99m}Tc$ | Labeled blood pool |
| Brain imaging procedures | $^{99m}Tc$ | Pertechnetate |
| Renal imaging procedures | $^{99m}Tc$ | Chelated complex with DTPA |
| Bone imaging | $^{99m}Tc$ | Methylenediphosphonate |
| Liver/spleen (RES) imaging | $^{99m}Tc$ | Colloidal preparations |
| Liver/gallbladder imaging | $^{99m}Tc$ | Iminodiaceticacid derivative |
| Lung perfusion imaging | $^{99m}Tc$ | Macroaggregated albumin |
| Lung ventilation imaging | $^{133}Xe$ | Gas |
| Thyroid therapy | $^{131}I$ | Sodium iodide |
| Polycythemia vera treatment | $^{32}P$ | Sodium phosphate |

[a] Reprinted from [2].

selective and relevant (i.e., characteristic and diagnostically important information should result from the image of its density distribution). Thus design and development of radiopharmaceuticals are an integral part of nuclear medicine. Table VI gives an overview of some of the most commonly used radioisotopes and their diagnostic applications.

A major problem of nuclear medicine results from the short half-lives of some of the elements used and the necessity of producing the radionuclides close to the site of patient administration. To solve this problem, medical cyclotrons have been developed. These are characterized by ease of operation, reliability, small size, and relatively low cost so that they can be installed and operated in hospitals. Radionuclides are produced by bombarding stable nuclides with cyclotron-accelerated high-energy particles [24].

## Clinical Applications E

Numerous procedures are currently used in nuclear medicine imaging (NMI) diagnostics. Due to rapid progress in the development of radiopharmaceuticals, the number of physiological processes being monitored expands constantly. Table VI gives a compressed summary of common radionuclear procedures.

The advantages and shortcomings of NMI can be noted in a highly specific procedure such as the measurement of glucose metabolism in the brain. The quantitative measurement of brain glucose metabolism involves the use of a labeled tracer, 2-deoxy-D-glucose, which mimics glucose and is transported across the blood–brain barrier by the same mechanism as glucose. Typical tracers have been prepared by labeling deoxyglucose with fluorine-18 to produce $^{18}$F-2-fluoro-2-deoxy-D-glucose and carbon-11 to produce 1-$^{11}$C-2-deoxy-D-glucose.

Once in the brain the compounds are phosphorylated to 2-deoxy-D-glucose-6-phosphate by the same enzyme that operates on glucose. However, the next step of glucose metabolism is blocked for the deoxy compound because glucose phosphate isomerase does not recognize the deoxy compound as a substrate. Thus the deoxy compound is trapped in the tissues of the brain. The PET scan can measure the rate of uptake of the labeled tracer and map its distribution. By measuring the relative concentrations of glucose and deoxy-glucose in arterial plasma, one can then calculate the glucose metabolic rate for the tissue under examination.

In spite of the formidable performance of radioisotope imaging, there is one important point in which it is inferior to magnetic resonance imaging of metabolic processes: In contrast to MRI, radionuclear imaging is not sensitive to the chemical bonds of an element, so chemical conversions cannot be imaged directly as with MRI. In the above example, MRI would be able to sense directly the various bonds of the tracer atoms and thus follow the steps of glucose metabolism without the further need of invasive blood sampling.

Radiopharmaceuticals may be involved in physiological processes and be transferred among various structures, but NMI, will notice only when the tracer element is enriched or removed from the area under study. This drawback is compensated at least partially by the fact that MRI is limited to the imaging of only a few elements, whereas NMI imaging is provided with a large number of highly specific radiopharmaceuticals. In addition, it is sensitive to much lower densities of gamma-ray sources.

## V ULTRASONIC IMAGING

### A Introduction

Ultrasonic (US) imaging techniques have proven to be valuable additions to the armament of imaging modalities that the physician can use in the visualization of internal structures and the diagnosis of disease. US imaging is the only medical imaging technique that does not use electro-

magnetic waves as the information carrier or measuring probe but instead is based on the propagation characteristics of mechanical, elastic waves in the body. As a consequence, it offers information that is complementary to that of other modes and often serves as a second imaging technique.

US imaging is commonly used for diagnosis of cysts and tumors, measuring blood flow, analysis of the cardiac cycle, diagnosis of carotid artery disease, evaluation of fetal development, as well as applications in neurology and opthalmology [30,31].

Ultrasound within the diagnostically relevant range of frequency and intensity is considered to be completely safe—no adverse biological effects have been reported—offering a significant advantage over other imaging techniques. In addition, the equipment is inexpensive compared with MRI, NMI, and radiography.

Sound and ultrasound are the same type of acoustic wave. The difference is in the physiology of human sound sensation, which separates audible sound from the higher-frequency inaudible ultrasonic waves (those above about 20 kHz). The common range of diagnostic ultrasound is from about 1 MHz for abdominal scans to about 20 MHz for ophthalmic examination. Average power levels are of the order of 0.01 to 200 $mW/cm^2$.

Images of internal structures of the human body are produced by transmitting short pulses of ultrasound into the body and recording the echoes from tissue interfaces. Such echo sounding is used by bats and dolphins for orientation, and accordingly the first technical applications were for underwater depth sounding and detection of submarines (SONAR), the equivalent of the radiowave detection system RADAR. Image formation is based on amplitude and time delay of the echoes. Reflections are observed wherever a change of the characteristic impedance of the medium occurs. These reflections and the ease of measuring an echo's running time (i.e., the distance of the reflecting interface), which is due to the lower speed of US propagation (about 1550 m/sec) make image formation simpler than in electromagnetic wave imaging devices. Detection of movements of structures and blood flow uses the Doppler shift of the reflected wave. Newest developments in US systems even use tomographic transmission techniques, resulting in additional information about structure and characteristic properties of the imaged tissue.

A multitude of imaging modes are used, distinguishable by the spatial dimension of the measurement, time dependency, and the transducer techniques used. Amplitude (A) scans display amplitude and running time of the echoes in only one dimension (i.e., along a single US beam). Timely changes of tissue location or geometry (e.g., heart valves) can be monitored by repetitive A scans of the same area, the single traces being displayed in parallel along the time axis. Another imaging mode that is used for movement detection is the Doppler technique, using either continuous or pulsed monochromatic waves, and recording the frequency

shift observed in the echo from a moving target. Adding a second spatial dimension to the measurements by mechanical or electronic beam shifts, thus scanning within a plane, results in a 2-D image of a body section. Because in this mode the echo amplitude modulates the intensity of the screen, it is called brightness (B) mode. This scanning technique is also able to provide 3-D imaging when the ultrasonic beam is directed to cover a volume element of the body. A final example involves real-time B-mode displays, which are used for imaging movement of structures and are displayed at frame rates up to 60/sec. Many different scanning systems and transducer arrangements have been developed for real-time systems.

The preceding ultrasound techniques can be used singly or in combination; so not only can a tomographic image be formed but also very accurate dimensional measurements can be made using an A-scan feature, and blood flow can be estimated for specific areas by Doppler techniques—all in a single noninvasive examination.

## B Physics of Ultrasound

### *1 Generation of Ultrasound*

The transducers used in diagnostic ultrasound are piezoelectric ceramics. The piezoelectric effect is an inherent property of crystals with polar electric axes. Deformation by mechanical pressure or strain applied in certain directions causes electrical polarization of the crystal, which is detectable by the resulting electric charges at the ends of the axes. The polarity and magnitude of the charges depend on the direction and amount of stress, strain being considered as negative pressure. The converse effect is also observed in such crystals: The application of an electric field to such a crystal produces mechanical deformation. If the elastic limits of the material are not exceeded, the charge densities produced are directly proportional to the strain in the crystal and vice versa. This means that the transducers can be used both to transmit and to receive sound waves.

Monocrystals of many compounds exhibit piezoelectric properties. Quartz, tourmaline, Rochelle salt, ammonium dihydrogen phosphate, and lithium sulfate have all been used for many years as electromechanical transducers. More recently, polycrystalline ceramic materials such as barium titanate, lead zirconate titanate (PZT), and the polymer polyvinylidene difluoride (PVDF) have come into use.

Ultrasound is generated by exciting vibrations of the piezoelectric transducer by an alternating electric field of appropriate frequency. The vibrations of the crystal are transmitted to any surrounding elastic material, resulting in the propagation of an ultrasonic wave that is bound to

longitudinal vibrations in biological tissue. The generation of ultrasound is most efficient when the transducer is excited at the resonant frequency of the crystal, which is determined by its size and shape. The converse piezoelectric effect allows the registration of ultrasound. When an acoustic wave hits the transducer, the pressure waves cause the crystal to vibrate, causing a changing voltage to be measured across the crystal. The sensitivity is highest at its resonant frequency.

## *Propagation of Ultrasound* 2

Propagation of ultrasound is best described by the Huygens–Fresnel principle of elementary wave generation. Certain properties, such as reflection and refraction by tissue interfaces, can also be depicted by the laws of geometric optics. Determination of diffraction and interference phenomena, however, requires the application of wave theory [28,29].

The intensity of an acoustic wave propagating in a homogeneous medium shows a steady decrease due to absorption, divergence of the sound beam, and scattering. Absorption is caused by hysteretic losses, viscous losses, thermal conduction leading to irreversible heat exchange between regions of high and low pressure, and thermal relaxation. These effects, which convert part of the acoustic energy to heat, increase toward higher frequencies of sound, leading to an augmented absorption coefficient $\beta$. The contribution of hysteretic loss is directly proportional to frequency, whereas the other terms are proportional to the square of the frequency. Intensity $I_x$ of the wave decreases exponentially with the length of path $x$. With $I_0$ being the intensity for $x = 0$, the intensity of the wave as a function of $x$ is given by

$$I_x = I_0 \exp(-\beta x) \tag{46}$$

Commonly, the absorption coefficient for a single frequency range is defined as

$$\beta = \frac{10 \log(I_0/I_x)}{x} \, dB/m \tag{47}$$

Both magnitude and frequency response characteristic of the observed absorption coefficients are dependent upon the kind of tissue. Some soft tissues are even anisotropic; for example, muscle has different $\beta$ values depending on the muscle fiber orientation relative to the US beam.

Beta/frequency lies in the range 0.5–3.5 (dB/cm)/MHz for soft tissue. For bone, beta/frequency is proportional to the frequency of the ultrasound, and the absorption coefficient is an order of magnitude higher than for soft tissues. Table VII gives some typical values of beta/frequency for biological materials. An alternative representation for attenuation data is

**TABLE VII**

**Typical Values of Beta/Frequency for Biological Materials of Clinical Ultrasound Frequencies**

| | Frequency dependence, B/f [(dB/cm)/MHz] | Half-value thickness, HVT (cm) |
|---|---|---|
| Blood | 0.18 | 16.7 |
| Fat | 0.63 | 4.8 |
| Brain | 0.85 | 3.5 |
| Skull Bone | 20 | 0.2 |
| Kidney | 1.0 | 3.0 |
| Liver | 0.94 | 3.2 |
| Muscle along fiber | 1.3 | 2.3 |
| Muscle across fiber | 3.3 | 0.9 |
| Heart muscle | 1.8 | 1.7 |
| Lung | 41 | 0.1 |
| Aqueous or vitreous Humor | 0.1 | 30.1 |
| Lens | 2.0 | 1.5 |

as half-value-thickness (HVT) figures. The HVT is the path length through the medium that reduces the beam to 50% of its original intensity. Table VII also shows selected values of HVT. Penetration depth is a very important parameter since it determines the spatial range of imaging.

As a general rule is it difficult to image structures deeper than 200 wavelengths below the surface. For example, the wavelength of 1-MHz US is 0.154 cm in tissue, which gives a useful range of about 30 cm (approximately 1 ft). For 5 MHz, for which the wavelength is 0.031 cm, the range is reduced to 6 cm.

## 3 *Reflection and Transmission*

Specific acoustic impedance $Z$ is defined as the ratio of pressure $p$ to particle velocity $v$:

$$Z = p/v \tag{48}$$

A special case occurs for plane waves propagating in a nonabsorbing medium. The characteristic impedance is defined as

$$Z = \rho c \tag{49}$$

where $\rho$ is the density of the medium and $c$ the speed of sound in the medium. The unit of impedance is the Rayl (after Lord Rayleigh). Table VIII lists the characteristic impedances for various media along with their densities and the speeds of sound in the media.

TABLE VIII

**Values of Density ($\rho$), Speed of Sound ($c$), and Acoustic Impedance ($Z$) for Various Substances at Clinical Ultrasound Frequencies**

| | $\rho$ (kg/m$^3$) | $c$ (m/sec) | $Z$ (kg/m$^2$ · sec) |
|---|---|---|---|
| Air | 1.29 | $3.31 \times 10^2$ | 430 |
| Water | $1.00 \times 10^3$ | $14.8 \times 10^2$ | $1.48 \times 10^5$ |
| Brain | $1.20 \times 10^3$ | $15.3 \times 10^2$ | $1.56 \times 10^5$ |
| Muscle | $1.04 \times 10^3$ | $15.8 \times 10^2$ | $1.64 \times 10^5$ |
| Fat | $0.92 \times 10^3$ | $14.5 \times 10^2$ | $1.33 \times 10^5$ |
| Bone | $1.9 \times 10^3$ | $40.4 \times 10^2$ | $7.68 \times 10^5$ |

Consider sound waves passing from a medium of one characteristic impedance $Z_1$ to another $Z_2$ (Fig. 25). The ratio of reflected intensity to incident intensity $\alpha_r$ is given by

$$\alpha_r = \frac{(Z_2 - Z_1)^2}{(Z_1 + Z_2)^2} \tag{50}$$

whereas the ratio of transmitted intensity to incident intensity $\alpha_t$ is

$$\alpha_t = \frac{4Z_1Z_2}{(Z_1 + Z_2)^2} \tag{51}$$

Note that $\alpha_r + \alpha_t = 1$.

If the two materials have similar impedances, as is the case with most biological tissue interfaces except tissue/bone, then only a small part of the incident beam will be reflected. However, when there is a large mismatch between the characteristic impedances as for the interface tissue/air, then nearly complete reflection occurs with no energy transmission.

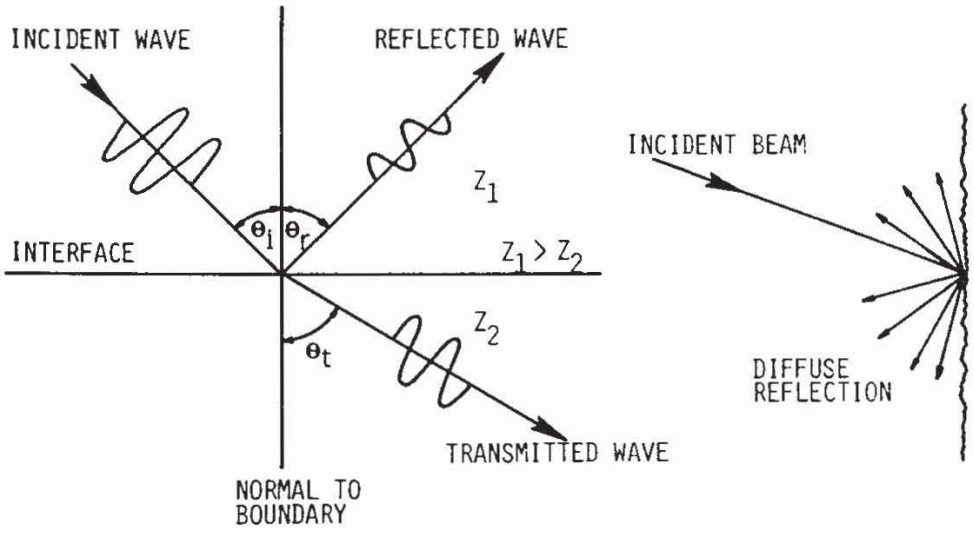


**Fig. 25.** Reflection and transmission of ultrasound.

The relevance of the impedance equations to scanning in medicine are (1) the ultrasound source must be coupled to the body using a fluid coupling medium that prevents air gaps or else very little of the sound energy is transmitted into the body; (2) reflections occur only when there is a change in impedance; and (3) shadows are cast by a good reflector such as bone and gas, which means that it is impossible to obtain an image from behind them.

Table IX lists characteristic impedance ratios for a range of biologically important tissues and the reflection coefficients between them.

Three types of reflection are observed in US imaging: specular reflection, diffuse reflection, and Rayleigh scattering.

**TABLE IX**

**Characteristic Reflection Coefficients[a] and Impedance Ratios[b] for Some Tissues**

| WATER | BLOOD | FAT | MUSCLE | LIVER | KIDNEY | SPLEEN | BRAIN | BONE |
|---|---|---|---|---|---|---|---|---|
| 0.014<br>1.028 | | | | | | | | |
| 0.040<br>1.084 | 0.054<br>1.114 | | | | | | | |
| 0.051<br>1.107 | 0.037<br>1.077 | 0.091<br>1.200 | | | | | | |
| 0.036<br>1.074 | 0.022<br>1.045 | 0.076<br>1.164 | 0.015<br>1.006 | | | | | |
| 0.033<br>1.068 | 0.019<br>1.038 | 0.073<br>1.157 | 0.018<br>1.037 | 0.003<br>1.006 | | | | |
| 0.042<br>1.088 | 0.028<br>1.058 | 0.082<br>1.179 | 0.009<br>1.018 | 0.006<br>1.012 | 0.009<br>1.019 | | | |
| 0.014<br>1.028 | 0.000<br>1.000 | * | * | * | * | * | | |
| 0.596<br>3.955 | 0.587<br>3.846 | * | * | * | * | * | 0.587<br>3.846 | |

[a] Upper value
[b] Lower value

1. Specular reflection is caused by planar interfaces, which reflect the echo at an angle equal to the angle of incidence; echo detection is possible only for perpendicular incidence.

2. Diffuse reflection occurs from rough surfaces on which the rough structures are approximately the same size as the wavelength of the incident wave (Fig. 25). Echoes are reflected back in all directions; so the transducer always detects an echo, even without perpendicular incidence. Due to the fanned echo beam, the amplitude of the echo of diffuse reflection is much smaller than for specular reflection; usually both types of reflections are present in ultrasonic imaging. In general, scattering-type diffuse reflections give a better visualization of structures than specular reflections.

3. Rayleigh scattering is observed in reflections from objects smaller than the wavelength of the incident beam, as occurs when US beam strikes a red blood cell. The object scatters the sound wave in all directions in the form of spherical waves. Thus both forward scattering and backscattering are observed, appearing as weak diffuse reflection and mainly as multi-directional diffraction or bending of the incident wave around the object. The echo rarely contributes to the image formation and the forward scattering causes divergence of the beam.

## *Transducers* 4

The basic element of an ultrasonic transducer is the piezoelectric crystal that both generates and detects the US. The acoustic field of the usually disk-shaped transducers, polarized so as to provide compression type vibrations, shows two distinct zones: the near field or Fresnel zone and the far field or Fraunhofer zone (Fig. 26). The near field is characterized by essentially parallel propagation of the ultrasonic wave. The beam begins to diverge in the far field, reducing the lateral resolution of an imaging system with increasing distance from the transducer. The unfavorable effect of far-field divergence can be avoided, at least partially, by focusing the sound waves with an acoustic lens or by using several transducers in a phased

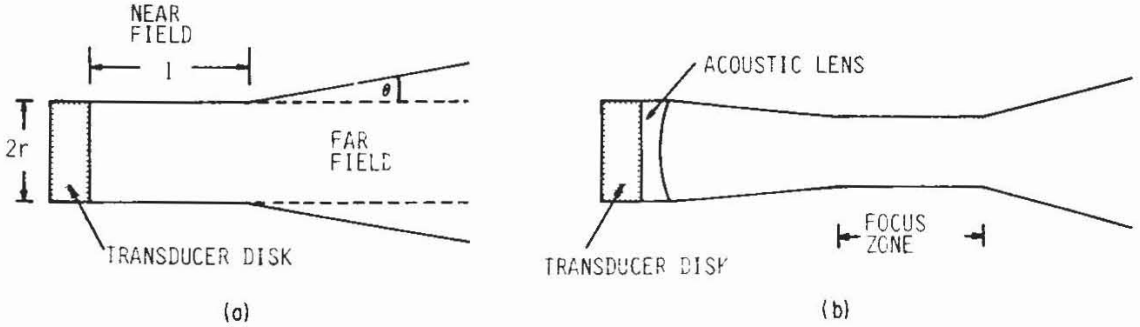


**Fig. 26.** (a) Ultrasound propagation from a transducer disk and (b) effect of focusing acoustic lens.

array, simulating the beam shaping of a lens. The near-field length $l$ is determined by the transducer radius $r$ and the wavelength $\lambda$ of the ultrasonic wave:

$$l = r^2/\lambda \tag{52}$$

The angle of divergence $\theta$ in the far field is

$$\theta = \arcsin 0.61\lambda/r \tag{53}$$

Since none of the known piezoelectric materials is matched acoustically with tissue, direct transducer/tissue interfaces exhibit reflection coefficients near one, resulting in very poor efficiency of sound transmission as well as insufficient sensitivity of echo recording. To improve the transducer performance, quarter-wave matching is applied. Essentially, this is done by placing a plastic material that has an acoustic impedance halfway between that of the piezoelectric crystal and the tissue in front of the transducer. With a thickness equal to one-fourth of the wavelength of the resonant frequency of the crystal, usually a ceramic, constructive interference between emitted and returning wave phases results in increased energy transfer in both directions.

The matching layer, which should be an odd number of quarter wavelengths thick at the frequency of operation, is chosen so that its characteristic impedance is the geometric mean of the characteristic impedances of the crystal and the medium. This scheme theoretically results in 100% transmission from the crystal to the medium. Thus

$$Z_{\text{matching layer}} = \sqrt{Z_{\text{crystal}}\, Z_{\text{medium}}} \tag{54}$$

For reasons of availability of suitable materials, often a multiple or graded matching layer approach is adopted.

In pulsed ultrasonic imaging modes, high longitudinal resolution requires the emitted pulse to be as short as possible. The common excitation of resonance, however, providing high energy conversion rates, causes the crystal to continue damped oscillation even after the desired pulse emission. The damping factor determines the effective pulse length. Providing suitable crystal backing material increases the damping factor and thus resolution.

Figure 27 shows the cross section of an ultrasound transducer suitable for pulse–echo or Doppler examinations. The crystal is mounted between a quarter-wave matching front plate and a backing layer that typically consists of 20 : 1 tungsten powder and epoxy resin, which absorbs all back radiation. A tuning coil is connected in parallel with the crystal mounting capacitance, thereby neutralizing the effect of this undesired capacitance on the resonant frequency of the crystal. For continuous wave use, the transducer is excited at its resonant frequency, which can be calculated from the speed of sound in the piezoelectric ceramic and its thickness. For example, in PZT the speed of sound $c$ is 4170 m/sec, which means that a

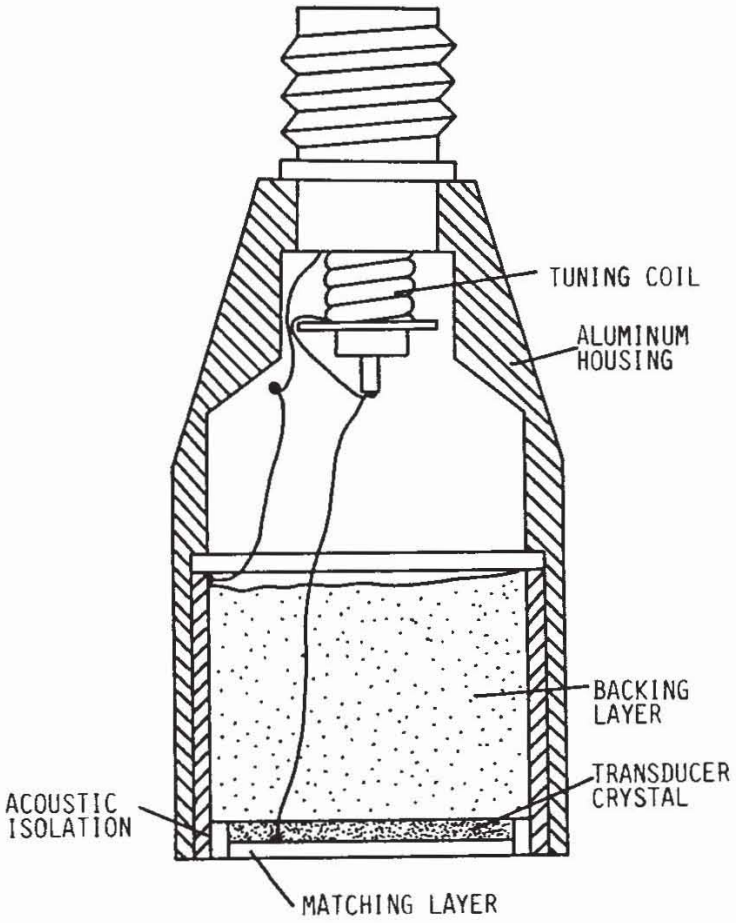


**Fig. 27.** Ultrasound transducer.

fundamental thickness mode resonance frequency $f$ of 1 MHz occurs for a half-wave thickness $d$ which yields

$$d = \frac{c}{2f} \tag{55}$$

$$d = \frac{4170 \times 10^3}{2 \times 10^6} = 2.085 \text{ mm} \tag{56}$$

For pulse mode operation the crystal is fed with a pulse whose duration is generally one-half the period of oscillation of the mounted crystal. After excitation the crystal rings for a few cycles, the number depending on the damping of the crystal.

## Ultrasound Scanning Modes C

### *Amplitude (A) Scan 1*

The A scan is based on the same principles as the pulse–echo techniques of range-finding radar or sonar. The transducer emits a pulse of ultrasound, and the time for the echoes to be reflected is measured. The

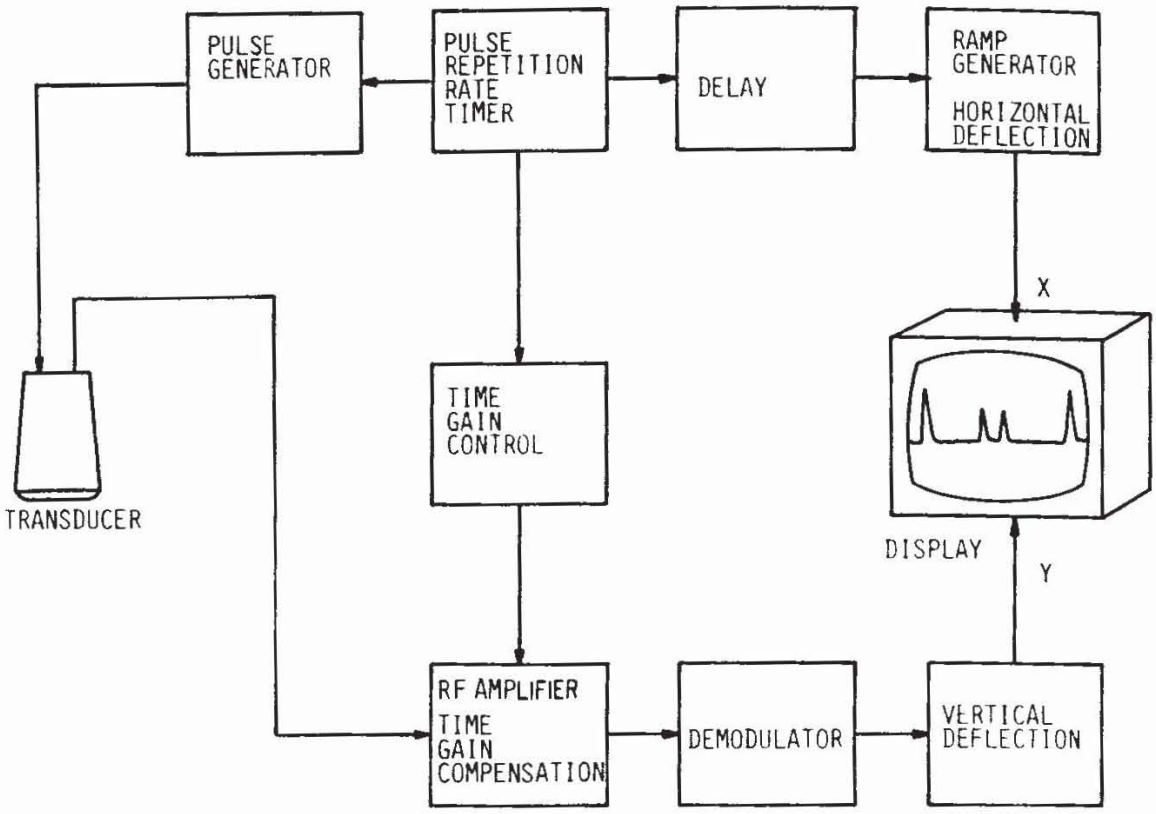


**Fig. 28.** A-scan block diagram.

cathode ray tube (CRT) display format shows echo traveling time or distance to tissue interfaces; The calculations are based on assumed constant sound velocity (shown horizontally) and the amplitude of the echo, a measure for the impedance mismatch (shown vertically).

Figure 28 presents a block diagram of the major components of an A scanner. A pulse repetition rate (PRR) timer triggers a pulse generator. After the pulse has been transmitted, the role of the piezoelectric crystal is switched to that of receiver. The echoes are detected, and the electrical signal is amplified by a radio-frequency (rf) amplifier whose gain is increased as a function of echo delay. The time gain compensation (TGC) generally provides an amplification factor that is exponentially increasing with time during a sweep, to compensate for the exponential attenuation of the echo by the tissue. The demodulator is usually a simple rectifier–envelope detector whose output drives the vertical deflection amplifier of the display. The PRR timer also triggers the display time base, which sweeps the trace proportional to time from left to right. A delay may be included so that a particular section of the display can be "zoomed" for more accurate distance measurements or better detail detection.

The maximum PRR is limited by the running time of the echoes and is related to the depth from which the furthest echo returns.

$$\mathrm{PRR}_{\max} = \frac{c}{2d} \tag{57}$$

where $c$ is the speed of sound in the medium and $d$ the depth of the furthest reflecting surface.

The two major diagnostic application areas for the A scan are echoencephalography for detection of shifts in the midline of the brain, and imaging in opthalmology. Figure 29 shows the encephalographic application in a cross section of a head. Pulses of ultrasound are transmitted into the relatively thin region of the skull just above the ear. The group of echo pulses at A are reflected from the proximal skull, cerebrospinal fluid, and meninges. The double echo at B is from the ventricle, which is normally near the middle of the brain. The echoes at C are from meninges, cerebrospinal fluid, and skull on the side of the head opposite the transducer. The procedure involves comparing the echo trace obtained when the transducer is positioned on the left side of the head with that obtained from the right side and determining whether or not a shift in the midline has occurred. A tumor or a hemorrhage on one side of the brain tends to shift the ventricle toward the opposite side. Generally a shift of more than 3 mm for an adult is considered abnormal.

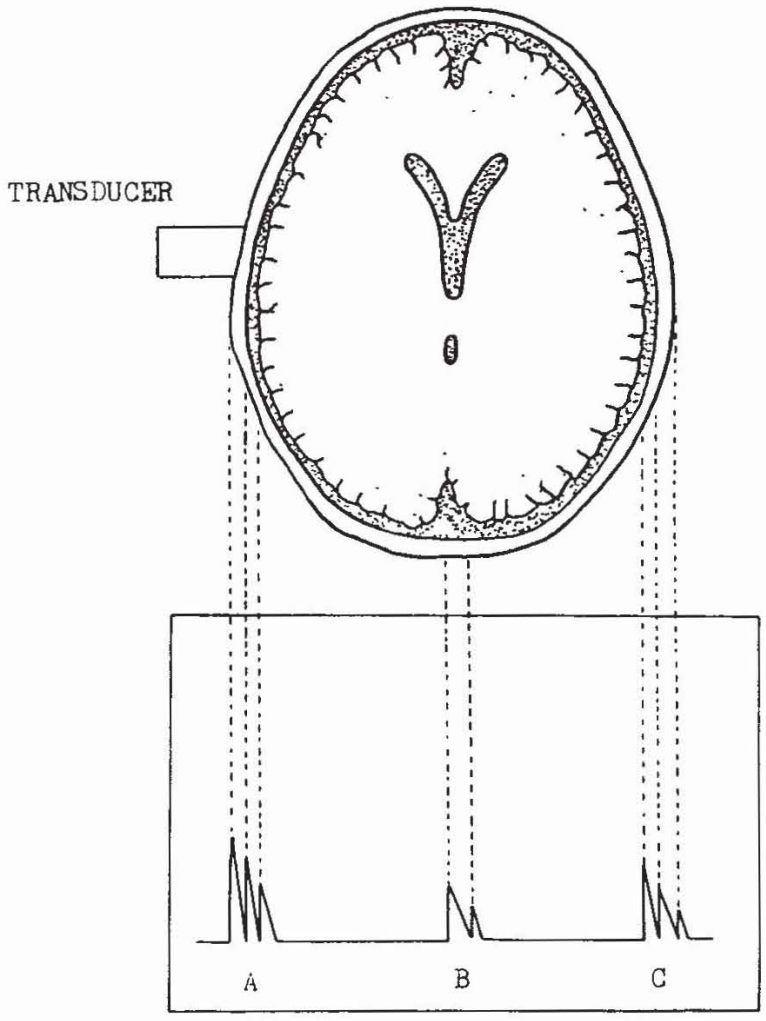


**Fig. 29.** Brain mid-line shift detection using an A scan.

Applications in opthalmology include the measurement of the distance between the cornea and the lens, lens thickness, and the distance from the lens to the retina. At 15 MHz the theoretical axial resolution is about 0.1 mm. Additionally, the A scan can diagnose detached retina even when the cornea, lens, or vitreous humor is too opaque for normal optical observation. Further applications are the evaluation of vitreous hemorrhage, ocular tumor, and foreign objects.

## 2 *Time–Motion (M) Scan*

The time-motion scan, usually abbreviated to M mode, is essentially a time-varying, repetitive A scan. The A-scan display can only show one line of information at a time. This drawback can be avoided if instead of displaying the amplitude of the echo along the vertical axis, one displays the echo amplitude as a brightness modulation. In this, a large reflection is displayed as a bright dot, its horizontal position corresponding to its running time or depth. The scan is then repeated without changing the location and direction of the transducer (i.e., the same body area is scanned again). The display of the recorded echo is shifted parallel to the first echo by an amount corresponding to the time interval between the two scans. Thus a time-dependent 2-D display is generated, in which the motion of objects is detected from the timely change of depth of the corresponding echo signal.

Figure 30 shows the block diagram of an M scanner. The structure is very similar to the A scanner except that the coordinates are rearranged so that depth is displayed vertically from top to bottom, echo intensity controls the trace brightness, and time is represented on the horizontal axis, advancing from left to right.

Echocardiography is a common application of M-mode scanning for obtaining diagnostic information about the dynamics of the heart. The places from where the heart can be probed are quite limited because of poor US transmission through lung tissue and bone. The usual procedure is to place the transducer between the ribs over the heart and to orient it at different angles to explore various regions of the heart. Thus it is possible to obtain information about the behavior of a particular valve or section of the heart.

A typical scan (Fig. 31) shows reflections from the chest wall (CW), the right (RVW) and left (LVW) ventricular walls, the interventricular septum (IVS), and the various valves, according to transducer orientation. In this figure the motion of the anterior (AL) and posterior (PL) mitral valve leaflets is displayed. The motion is correlated with the electrical activity of the heart (ECG) and the phonocardiogram (PCG) which can be recorded at the same time. Information of interest is about proper opening and closing of the mitral valve.

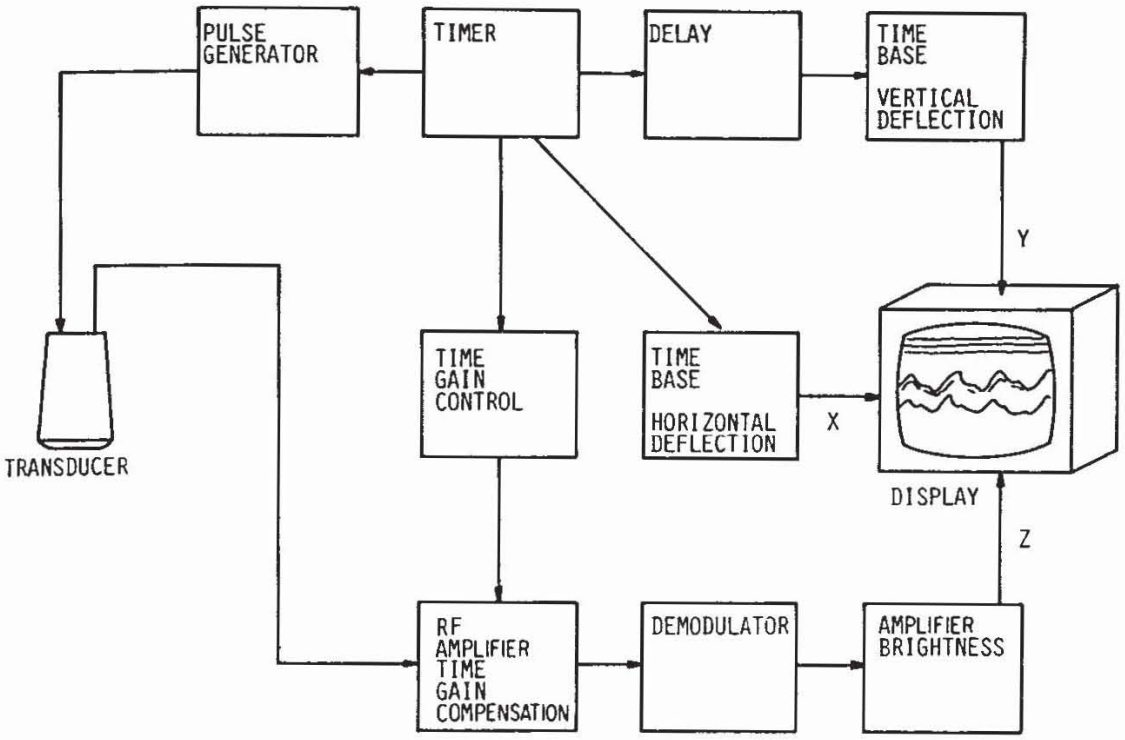


**Fig. 30.** Block diagram of an M scanner.

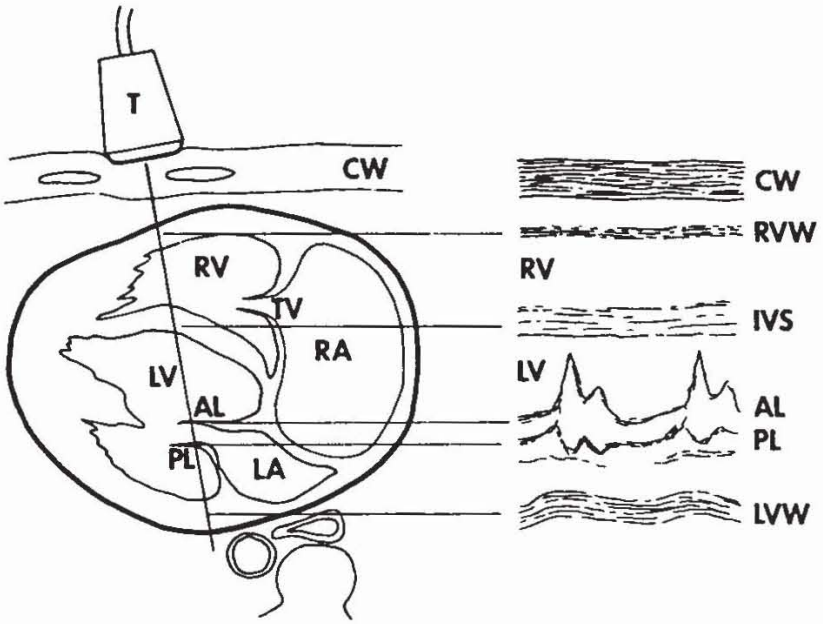


**Fig. 31.** Time-motion scan of heart valves. T, transducer; CW, chest wall; RV, right ventricle; IVS, interventricular septum; LV, left ventricle; AL, anterior mitral valve; PL, posterior mitral valve; LVW, left ventricular wall; TV, tricuspid valve; RA, right atrium; LA, left atrium.

Pericardial effusion can be easily detected with an M-mode scan. The pericardial sac surrounding the heart is normally in direct contact with the heart. An M-mode scan of a normal heart shows the anterior right ventricular wall in direct contact with the anterior pericardium and the stationary chest wall, and the posterior left ventricular wall in contact with

the posterior pericardium. When pericardial effusion occurs, the space between the heart and pericardium fills with a fluid that is relatively echo free, and an M-mode scan shows a separation between the sac and the heart both anteriorly and posteriorly. The same scan can be repeated periodically to follow the progress of the treatment.

## 3 Brightness (B) Scan

In the B-scan mode, echoes are detected for a range of different transducer positions. As in M scans, the echoes are displayed by brightness modulation. However, the time axis is replaced by a second spatial axis, indicating the position of the transducer. The two spatial coordinates, depth and transducer location, span a plane in the body, thus enabling 2-D reflectivity imaging of body sections. By sweeping the US beam across any arbitrary plane section, many sets of echo spots are obtained, and they combine to delineate the internal structures of the body.

To reconstruct the image it is necessary to know the transducer position and its orientation. The transducer is attached to either an articulated arm that allows a scan over a sector or a rectilinear gantry that produces a linear scan. Additionally, there is a compound mode (compound scan) that combines linear and sector scans and can provide better registration at the edges of internal structures. The transducer is coupled by shaft encoders and position sensors to the coordinate generator as shown in the block diagram of Fig. 32. The other blocks are similar to the M-mode scanner.

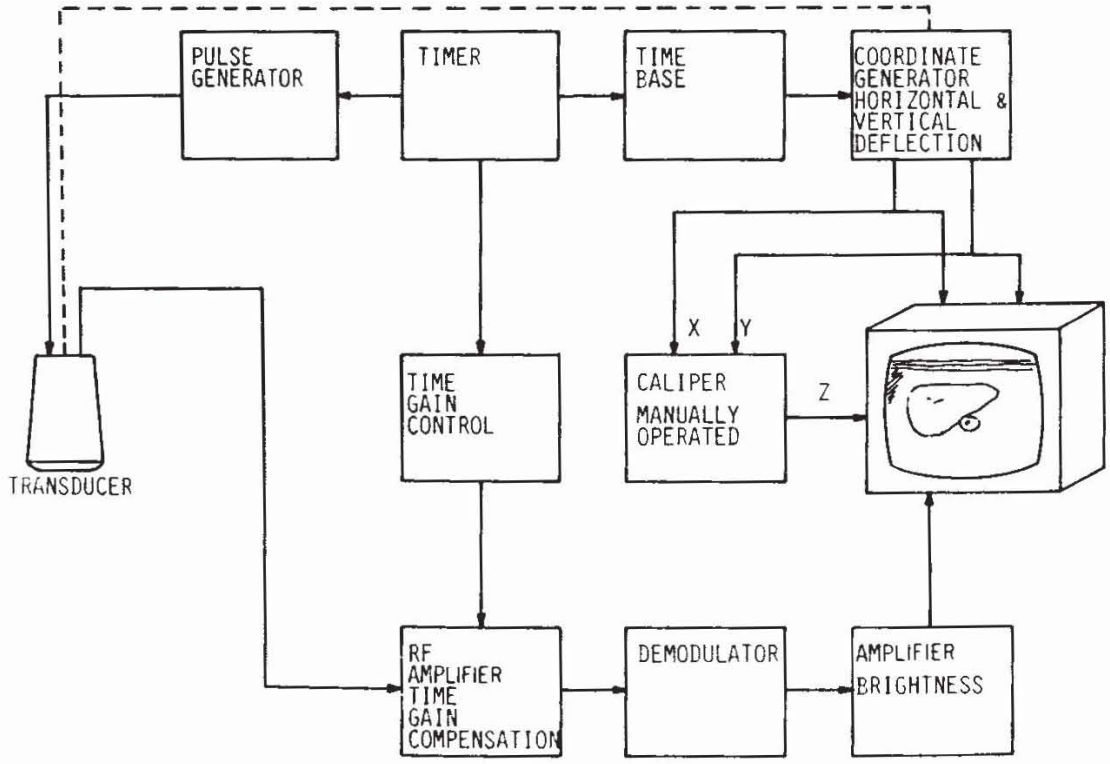


Fig. 32. B-scan block diagram.

An additional feature is provided by displaying arbitrary cursors and their distances, which allows very accurate dimensional measurements.

Instead of a CRT, the display unit is sometimes a normal video monitor fed from a scan converter. The random image lines are stored in a matrix that is then read so as to produce a video raster scan. The digital scan converter provides an image format, depending on the monitor used, of about 480 × 640 pixels. The advantages of the digital scan converter over its analog predecessors is that drift is eliminated and digital image storage and postprocessing are possible.

## *Real-Time Scan* 4

Real-time scanning sweeps the B-mode image plane so rapidly that the successive images provide an essentially continous view of even moving internal structures. Frame rates are achieved up to 60 images per second, guaranteeing flicker-free imaging [32].

Real-time scanners are divided into two major categories, mechanical and electronic scanners, both of which can be further subdivided. Mechanical scanners are categorized by the scanning motion: rectillinear, sector, spinner, and oscillating reflector. Figure 33 shows the types of motion used in mechanical real-time scanners. These have essentially replaced the compound B scan for almost all imaging.

Electronic scanners are divided into linear arrays and phased arrays [20]. A linear array may consist of a single row of 100 transducers, each 10 mm long by 1.5 mm wide, the whole array then being 150 mm long. More

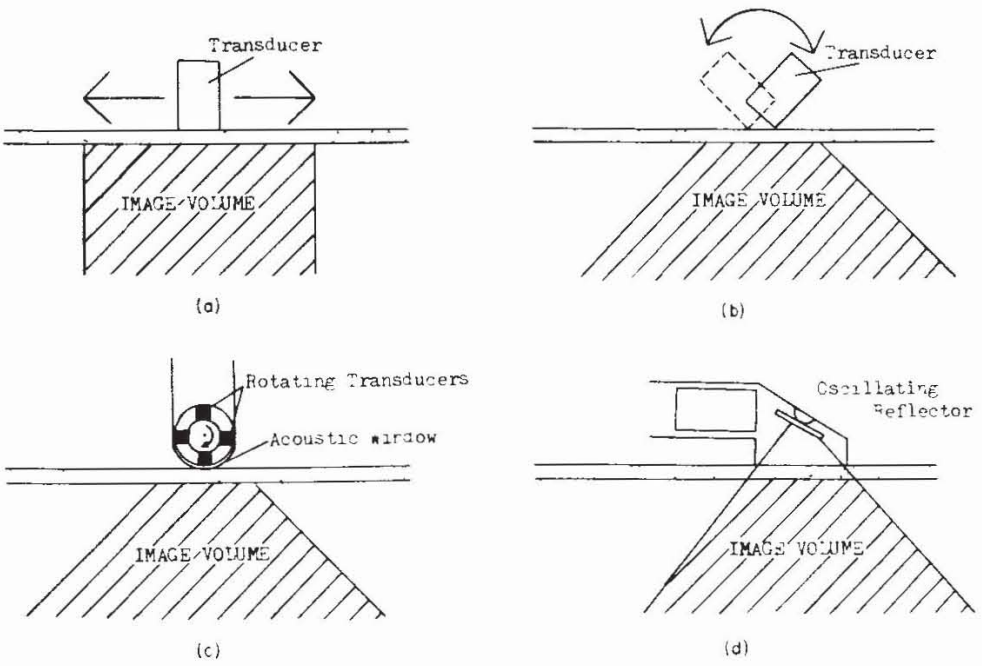


**Fig. 33.** Mechanical real-time scanners. (a) Rectilinear, (b) sector, (c) spinner, and (d) oscillating reflector.

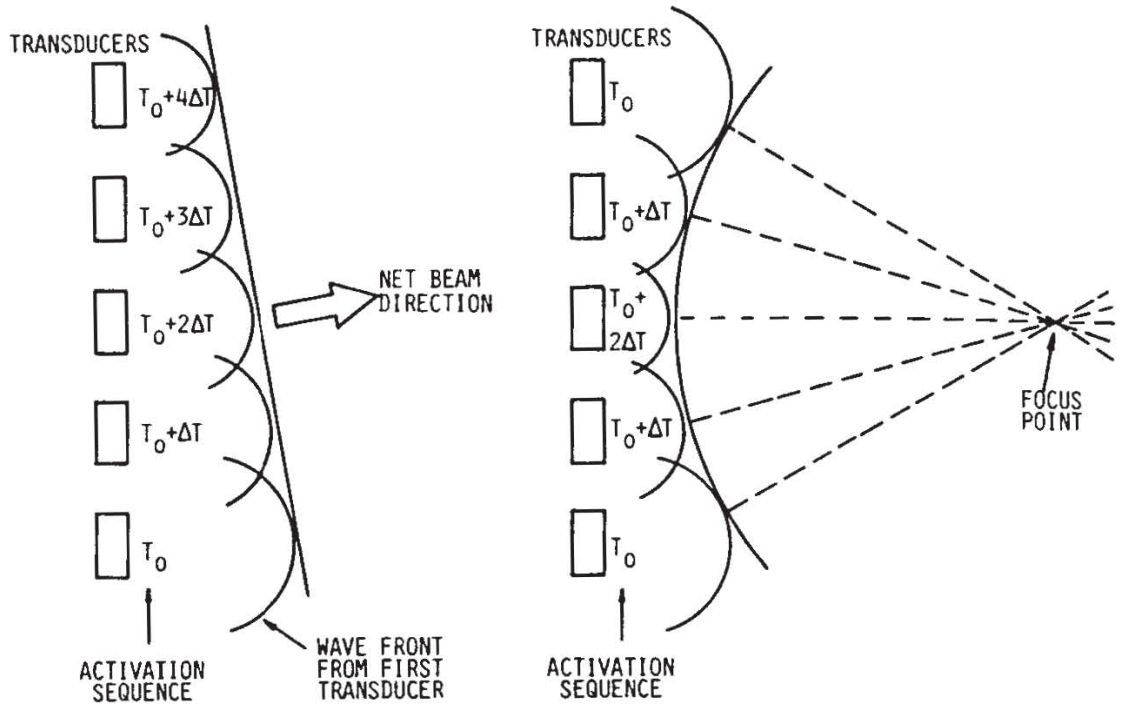


**Fig. 34.** Beam steering and focusing by delayed activation of a phased array transducer.

complex formats are possible, such as a 400-element rectangular array arranged into 100 groups of transducers of 4 elements each. A linear scan is produced by successively switching adjacent transducers on.

The ultrasonic phased-array scanner concept is derived from beam-steerable phased-array radar, which in turn can be understood in terms of the Huygens' principle of wave propagation. The transducer consists of about 32–64 elements arranged in a row. Using beam steering with superimposed dynamic focusing one can produce quality images over a $\pm 45°$ sector. To sweep the beam through a sector, the pulses to the elements are systematically delayed on transmission, as shown in Figure 34. For beam focusing, the central elements are excited with a delay against the outer element.

Phased array scanners, also used in circular arrangements [21], can provide two simultaneous M-mode displays as well as a full 2-D tomographic image.

## 5 *Doppler Measurements*

The Doppler effect is the apparent change in frequency of waves that occurs if either transmitter and detector are in relative motion or if the wave is reflected by a moving target. Detecting this frequency shift enables the registration of motion and flow.

Continuous-wave Doppler emits a constant beam of ultrasound and is capable of providing velocity information. Pulse Doppler can provide spatial information as well as velocity information.

The relevant shift equation is for a stationary source and moving target. The reflected echo frequency $f_e$ is related to the transmitted frequency $f_t$ by

$$f_e = f_t \frac{c - u}{c + u} \tag{58}$$

where $c$ is the speed of sound in the medium and $u$ the speed of the reflector away from the ultrasound probe. If the reflector is moving toward the probe, $u$ is negative, in which case the echo frequency is higher than the transmitted frequency.

The Doppler shift $f_d$ is defined as the difference between the transmitted and echo frequencies:

$$f_d = f_t - f_e = \frac{2f_t u}{c + u} \approx \frac{2f_t u}{c} \tag{59}$$

since $c \gg u$. The Doppler shift is either positive or negative, depending on the direction of the movement.

Figure 35 shows a block diagram for a Doppler US flowmeter. An oscillator feeds a power amplifier that drives the transmitting crystal. The amplified received signal is multiplied by the transmitted signal in a mixer that produces the sum and difference frequencies. Consider two cosine signals $\cos(t)$ and $\cos(e)$ that correspond to the transmitted and echo frequencies, respectively, multiplied together:

$$\cos(t)\cos(e) = \frac{\cos(t + e) + \cos(t - e)}{2} \tag{60}$$

Separation of the two spectral components is easily achieved by low-pass or high-pass filtering because of the large gap between their frequencies. With

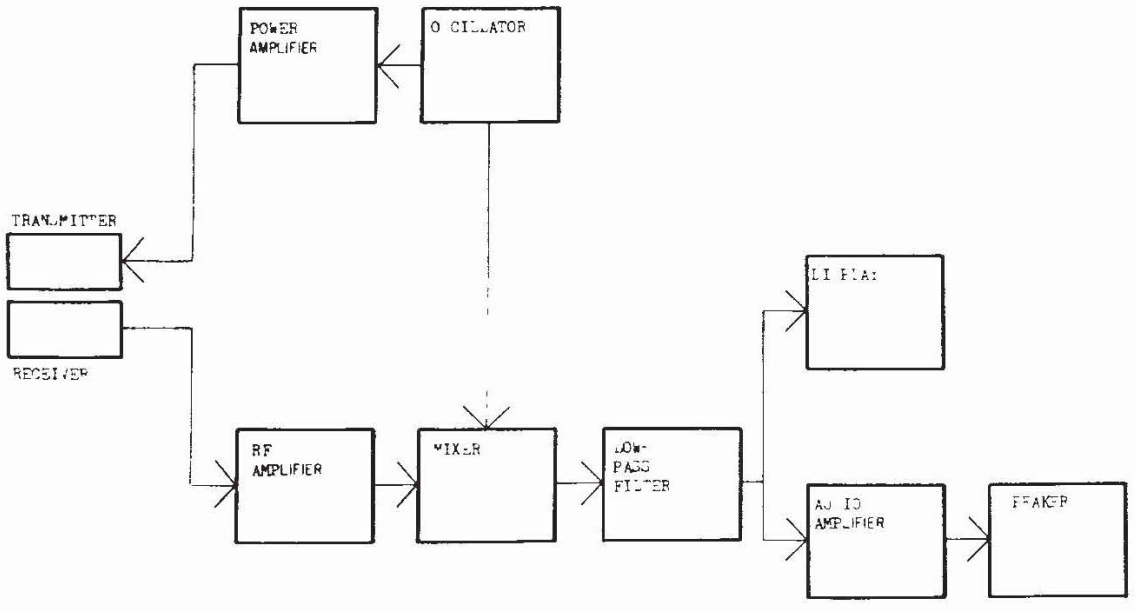


**Fig. 35.** Block diagram of a doppler ultrasound system.

a 5-MHz US wave and a typical Doppler shift in the range of ±1500 Hz, the sum frequency is 10 MHz ± 0.015%, whereas the difference frequency is given by the Doppler shift. Restricting signal analysis on the low-frequency component (LF), as is commonly done, means that the information on the direction of motion or flow is lost unless the phases of transmitted and received signals are compared, since the cosine is an even function, which does not allow differentiating between positive and negative frequencies. The low-frequency signal lies in the audio band for common US frequencies, and the physiological range of velocities is found. It is either displayed on an oscilloscope or fed to a loudspeaker for acoustic background surveillance.

Instead of mixing the echo signal with the true oscillator frequency, it is possible to shift that frequency slightly, providing an offset of the difference frequency. Its center frequency (i.e., without Doppler shift) is then transferred from 0 Hz (dc) to a frequency high enough to avoid negative difference frequencies caused by moving targets. In this case, directional information is preserved, which is the basis for directional Doppler instruments.

Pulsed Doppler systems can measure velocities at various depths by a process known as range gating. The receiver amplifier is turned on only after a period of time that corresponds to the running time from the transmitter to the target area and back to the receiver. In this way it is possible to build up information about flow profiles in vessels.

By combining pulse and directional Doppler techniques one can measure velocities, flow directions, flow profiles, and dimensions all in one instrument.

The main areas of application of Doppler US are in echocardiography, fetal heart rate measuring devices, and measuring blood flow in vessels. Refer to the chapter on non invasive diagnostic cardiology for further application information.

## 6 *Duplex Scan*

A logical extension of the various modalities discussed so far is to combine them in one instrument. The duplex scanner combines real-time 2-D imaging with a pulsed Doppler system for blood-flow studies. Once the region of interest has been identified by the operator on the real-time display, Doppler measurements can be taken.

## 7 *Supplementary Scanning Modes*

Ultrasonic imaging is not restricted to 1-D or 2-D echo techniques, providing information only on reflectivity boundaries. Ultrasonic computed tomography techniques have been developed, based on reflection,

transmission, or diffraction of ultrasound, that are able to display 3-D images of tissue absorption, reflectivity, speed of sound, and dispersion [16]. The main diagnostic potential of these techniques is in the imaging of areas that are inaccessible to simple echo techniques as well as in tissue characterization, thought to be of special value in the diagnosis of abnormal tissue (e.g., tumors). CT techniques used are the same as described in Section III—computed tomography.

## *Resolution* 8

Resolution of US imaging depends on three components that are all coupled indirectly: the two spatial components, axial and lateral resolution, which specify the size of the smallest picture element, and the amplitude resolution, which specifies the smallest differences of reflectivity that can be detected directly depending on the SNR of measured echoes.

Axial resolution (i.e., the ability to distinguish objects along the direction of the US beam) is given by the minimum distance between two objects that will result in separate, non overlapping echo pulses. This distance is half the spatial US pulse length, which is dependent on the frequency, the number of cycles in a pulse, and the velocity of sound in the imaged tissue. For soft tissue, the axial resolution is approximately

$$\text{axial resolution (mm)} = \frac{0.77 \text{ number of cycles in a pulse}}{\text{frequency (MHz)}} \tag{61}$$

Improved resolution can be achieved by increasing the transducer damping to reduce the number of cycles in each pulse or by increasing the frequency. However, the attentuation also increases with frequency, which forces a tradeoff between spatial resolution and SNR. Poor SNR ultimately degrades image quality, which means that high-frequency/high-resolution images can be obtained only for superficial structures or for organs that can be viewed via some low-attenuation window, such as a fetus in the amniotic fluid or certain structures through a full bladder. A further complication is the variability of the speed of sound in various tissues. For example, the speed of sound in compact bone is 3600 m/sec, which is more than twice as fast as the speed of sound in soft tissue. As a result, the axial resolution in bone is less than half that of soft tissue. Another consequence is that the variability of sound velocity leads to an erroneous display of distances in US reflection scans.

Lateral resolution (perpendicular to the beam direction) is limited by the beam width. Beam focusing can reduce the beam width over a certain distance. The degree of focusing can be matched to the frequency of the transducer and the expected depth of penetration.

Amplitude resolution is limited by two noise factors: electrical and speckle noise [11]. Unlike X-ray imaging, with its signal-dependent Poisson noise, US imaging is influenced by signal-independent additive Gaussian input noise that results mainly from the transducer and the first amplifier stage. This electrical noise leads to a decrease of resolution with increasing distance from the transducer since reflections from greater depths, which experience increased attentuation, result (with constant amplifier and transducer noise) in a reduced SNR. Speckle noise results from coherence properties of the US wave. Due to the finite spatial resolution of imaging, echoes are always received from a distribution of scatterers within the pixel. These signals add coherently (i.e., constructively and destructively depending on the relative phases of each scattered wave form). For a random distribution of scatterers and sinusoidal US waves, the SNR, defined as the ratio of the mean of the measuring signal envelope $E$ to its standard deviation $\sigma$ is always

$$\text{SNR} = \frac{\bar{E}}{\sigma} = 1.9 \tag{62}$$

It should be noted that this SNR does not depend on the signal amplitude. For physiological tissue structures SNR is somewhat better; however, speckle noise often overrides electrical noise and is a serious problem when imaging larger organs consisting of uniformly distributed scatters, such as the liver. Improved SNR can be achieved by averaging different images of the object with independent speckle patterns, as is done by compound scanners, combining different views of the same area.

## VI ENDOSCOPY

Despite the immense diagnostic potential of non invasive imaging procedures and the high standards of technical quality reached, not all medical needs are covered. So endoscopy is still of great importance in medical diagnostics and due to the combined therapeutic potential will maintain its rank as one of the most powerful medical imaging techniques. Endoscopy provides direct imaging of internal tissue surfaces that are accessible through natural body openings or small skin incisions.

Endoscopes either enable immediate views by optical systems or transmit high-resolution color TV pictures from a tip-mounted miniaturized camera. Optical systems are divided into two categories: rigid tubes which are restricted to rectilinear optical paths and flexible fiber optics which enable access even to hard-to-reach areas. The fiberscope (Fig. 36) contains two bundles of optical fibers, one guiding the rays of the light

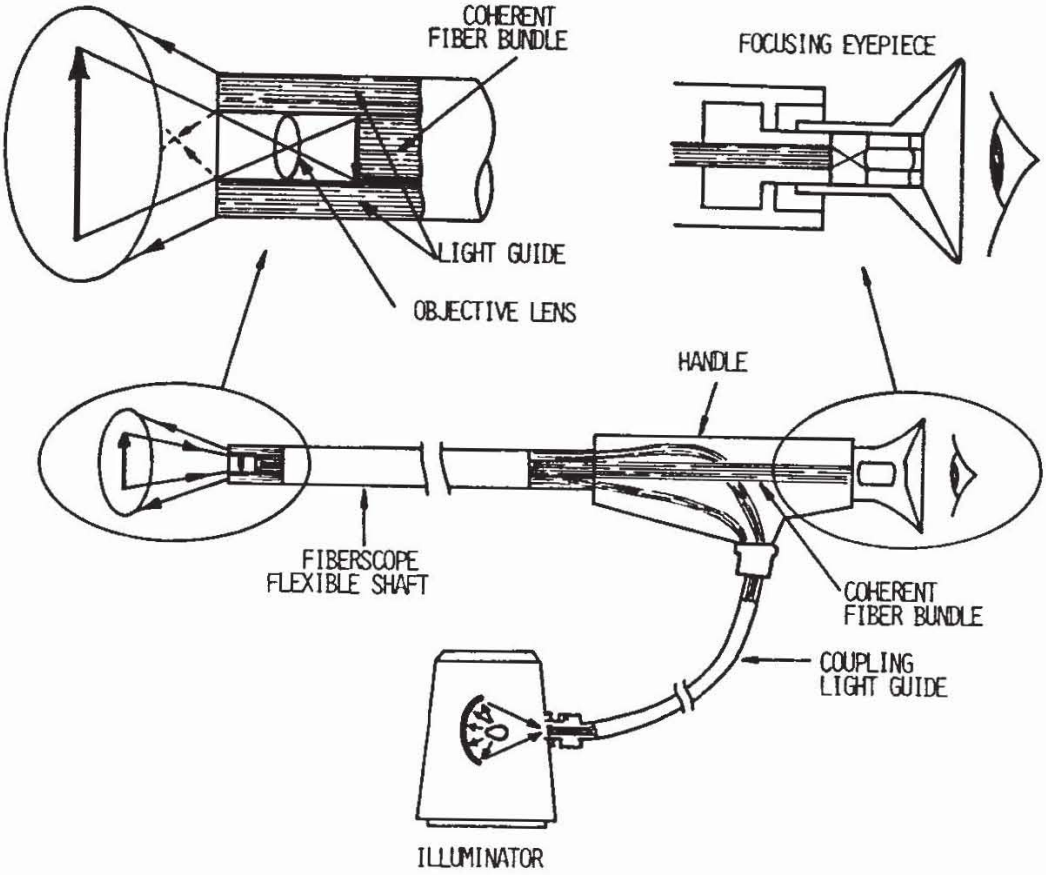


**Fig. 36.** Construction of a fiberscope.

source to illuminate the area of interest and the other transmitting the pictures. The imaging bundle consists of up to $10^6$ single fibers, each transmitting one louver cell of the point raster scanned picture. The diameter of the single glass fibers is in the range 5–50 $\mu$m, resulting in endoscope diameters of 4–10 mm. Light is transmitted within the glass core of the fibers by multiple total reflection at the interface to a lower refractive index glass cladding (Fig. 37). The main engineering problem is the small numerical aperture of the fibers (i.e., the solid angle from which light is accepted), which limits both the area of view and the light intensity. Improvements can be achieved by conical cuts of fiber tips.

Therapeutic tools implemented in endoscopes include, among others, laser optics for small surgical manipulations, electrodes for high-frequency coagulation, forceps for biopsy, wire nooses to remove foreign objects and

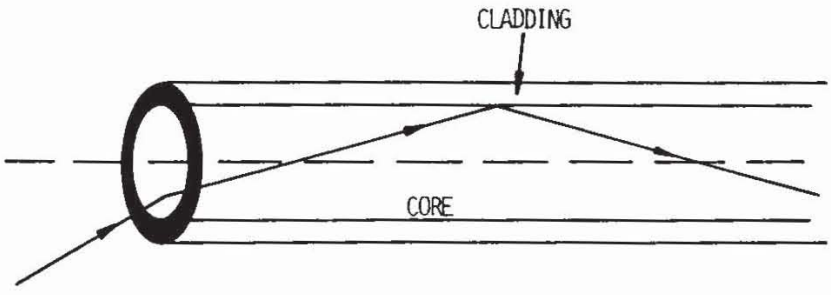


**Fig. 37.** Light transmission of an optical fiber by total reflection.

smashing stones, shock-wave transmitters for stone splitting, and suction pipes. The main diagnostic applications are given in Table X. Specific advantages of endoscopy compared to radiography are shown in Table XI.

**TABLE X**

**Types and Uses of Endoscopy**

| | |
|---|---|
| Endoscopy | |
| Without operative incisions | With small operative incisions |
| Esophagoscopy | Laparoscopy |
| Gastroscopy | Thoracoscopy |
| Duodenoscopy | Mediastinoscopy |
| Enteroscopy | Retroperitoneoscopy |
| Rectoscopy | Arthroscopy |
| Rectosigmoidoscopy | Arterioscopy |
| Sigmoidocoloscopy | |
| Bronchoscopy | |
| Cystoscopy | |
| Laryngoscopy | |
| Endoscopy of nasal sinuses | |
| Amnioscopy | |
| Diagnostic possibilities | |
| Visual inspection (e.g., tumor, ulcer, inflammation, lesion, and bleeding) documentation by photography | |
| Obtaining tissue for biopsy | |
| Obtaining liquids for bacteriologic and/or cytologic examination | |

**TABLE XI**

**Comparative Advantages of Endoscopy and Radiography**

| X-ray | Endoscopy |
|---|---|
| More clearly arranged presentation of larger areas (especially important for surgeons) | Better resolution |
| | Differences in color which facilitate detection and localization of small lesions |
| Bowel movement disorders better recognizable | Extraction of bioptic and cytologic material |
| Better estimation of the extension of a stenosis | Destruction of stones |
| Better estimation of fistula and diverticula | Better for diagnostics in gastrointestinal emergencies |
| Valuation of whole organ often possible in spite of stenosis | High therapeutic potential |

## REFERENCES

1 Macovski, A. "Medical Imaging." Prentice-Hall, Englewood Cliffs, New Jersey, 1983.
2 Bronzino, J. D "Biomedical Engineering and Instrumentation" PWS Engineering, Boston, Massachusetts, 1986.

3. Nalcioglu, O., and Cho, Z. H., eds. "Selected Topics in Image Science." Springer-Verlag, Berlin and New York, 1984.
4. Brooks, R. A., and Di Chiro, G. Principles of computer assisted tomography (CAT) in radiographic and radioisotopic imaging. *Phys. Med. Biol.* **21,** 689–732 (1976).
5. A. C. Kak, computerized tomography with x-ray, emission, and ultrasound sources. Proc. *IEEE* **67,** 1245–1272 (1979).
6. R. E. Alvarez and A. Macovski, Energy-selective reconstructions in x-ray computerized tomography. *Phys. Med. Biol.* **21,** 733–744 (1976).
7. H Anger, Scintillating camera with multichannel collimators. *J. Nucl. Med.* **5,** 515 (1964).
8. W. H. Blahd, "Nuclear Medicine." McGraw-Hill, New York, 1965.
9. R. N. Bracewell, "The Fourier Transform and Its Application." McGraw-Hill, New York, 1965.
10. R. A. Brooks and G. Di Chiro, Statistical limitations in x-ray reconstructive tomography. *Med. Phys.* **3,** 237–240 (1976).
11. C. B. Burckhardt, Speckle in ultrasound B-mode scans. *IEEE Trans. Sonics Ultrason.* **SU-25,** 1–6, (1978).
12. Chesler, D. A., Riederer, S. J., and Pelc, N. J. Noise due to photon counting statistics in computed x-ray tomography. *J. Comput. Assist. Tomogr.* **1,** 64–74 (1977).
13. Z. H. Cho, Special issue on physical and computational aspects of 3-dimensional image reconstruction. *IEEE Trans. Nucl. Sci.* **NS-21** (1974).
14. F. T. Farmer and M. P. Collins, A new approach to the determination of anatomical cross-sections of the body by Compton scattering of gamma-rays. *Phys. Med. Biol.* **16,** 577–586 (1971).
15 R. M. Gray and A. Macovski, Maximum A-posteriori estimation of position in scintillation cameras. *IEEE Trans. Nucl. Sci.* **NS-23,** 849–852 (1976).
16. J. L. Greenleaf and R C. Bahn, Clinical imaging with transmissive ultrasonic computerized tomography. *IEEE Trans. Biomed. Eng* **BME-28,** 177–185 (1981).
17. G. T. Herman, "Image Reconstruction from Projections." Academic Press, New York, 1980.
18. B. K. P. Horn, Density reconstruction using arbitrary ray-sampling schemes. *Proc. IEEE* **66,** 551–562 (1978).
19. E. J. Johns and J. R. Cunningham, "The Physics of Radiology." Thomas, Springfield, Illinois, 1974.
20. A. Macovski, Ultrasonic imaging using arrays. *Proc. IEEE* **67,** 484–495 (1979).
21. A. Macovski and S. J. Norton, High resolution B scans using a circular array. *Acoust. Hologr.* **6,** 121–143, (1975).
22. P. J. Ell and B. L., Holmann, eds. "Computed Emission Tomography." Oxford Univ. Press, London and New York, 1982.
23 J G. Kereiakes and M Rosenstein, "Handbook of Radiation Dose in Nuclear Medicine and Diagnostic X-Ray." CRC Press, Boca Raton, Florida 1980.
24. E. Lebowitz and P Richards, Radionuclide generator systems. *Semin Nucl. Med.* **4,** 257–268 (1974).
25. J. A Sorenson and M. E. Phelps, "Physics in Nuclear Medicine " Grune & Stratton, New York, 1980.
26. E. Tanaka, Generalized correction functions for convolutional techniques in three-dimensional image reconstruction *Phys. Med Biol.* **24,** 157–161 (1979).
27 M M. Ter-Pogossian *et al.* A positron-emission transaxial tomograph for nuclear imaging (PETT). Radiology **114,** 89–98 (1975).
28. P. N T Wells, "Physical Principles of Ultrasonic Diagnosis " Academic Press, New York, 1969.
29. P. N. T. Wells, "Biomedical Ultrasonics." Academic Press, New York, 1977
30. M. De Vlieger, ed. "Handbook of Clinical Ultrasound " Wiley, New York, 1978.

31. S. L. Hagen-Ansert, "Textbook of Diagnostic Ultrasonography." Mosby, St. Louis, Missouri, 1983.
32. O. R. Keil, Ultrasound and its various modes in use, Part II: Real-time scanners. *Med. Instrum.* **16**(2), (1982).
33. H. Barrett and W. Swindell, "Radiological Imaging." Academic Press, New York, 1981.
34. B. Hamilton, ed. "Medical Diagnostic Imaging Systems." F&S Press, New York, 1982.
35. J. G. Webster, ed. "Medical Instrumentation—Application and Design." Houghton, Boston, Massachusetts, 1978.